Supporting Information

High-Performance Elastomeric Lithium Metal Anodes Enabled by a Lithiophilic Monolayer-Assembled Nano-Crumpled Micro-Concave Architecture

Sungha Choi[§], Donghyeon Nam[§], Geon Choi[§], Seonho Lee, Seungeun Paik, Yongkwon Song, Seungyeop Choi, Jaejin Lim, Woojae Chang, Jeong Gon Son, Daegun Kim, Giwon Lee, Sungjun Park, Yong Min Lee, Seoin Back[*] Yongmin Ko, and Jinhan Cho**

S. Choi, S. Lee, W. Chang, Prof. J. Cho

Department of Chemical and Biological Engineering, Korea University, 145 Anam-ro, Seongbuk-gu, Seoul 02841, Republic of Korea

E-mail: jinhan71@korea.ac.kr

D. Nam

The George W. Woodruff School of Mechanical Engineering, Georgia Institute of Technology, Atlanta, Georgia 30332, USA

G. Choi, J. G. Son, Prof. S. Back, Prof. J. Cho

KU-KIST Graduate School of Converging Science & Technology, Korea University, 145 Anam-ro, Seongbuk-gu, Seoul 02841, Republic of Korea

E-mail: sback@korea.ac.kr

S. Paik

Department of Mechanical Engineering, Seoul National University, 1 Gwanak-ro, Gwanak-gu, Seoul 08826, Republic of Korea

Y. Song

Department of Materials Science and Engineering, Northwestern University, Evanston, IL 60208, USA

S. Choi, J. Lim, Prof. Y. Lee

Department of Chemical and Biomolecular Engineering, Yonsei University, Yonsei-ro 50, Seodaemun-gu, Seoul 03722, Republic of Korea

J. G. Son, Prof. J. Cho

Soft Hybrid Materials Research Center, Korea Institute of Science and Technology (KIST), 5 Hwarang-ro 14-gil, Seongbuk-gu, Seoul 02792, Republic of Korea

Prof. D. Kim

School of Chemical, Biological and Battery Engineering, Gachon University, 1342 Seongnam-daero, Sujeong-gu, Seongnam 13120, Republic of Korea

Prof. G. Lee

Department of Chemical Engineering, Kwangwoon University, 20 Kwangwoon-ro, Nowon-gu, Seoul 01897, Republic of Korea

Prof. S. Park

Department of Intelligence Semiconductor Engineering, Ajou University, Suwon 16499, Republic of Korea

Department of Electrical and Computer Engineering, Ajou University, Suwon 16499, Republic of Korea

Prof. S. Back

Institute for Multiscale Matter and Systems (IMMS), Ewha Womans University, Seoul 03760, Republic of Korea

Y. Ko

Division of Energy & Environmental Technology, Materials Research Institute, Daegu Gyeongbuk Institute of Science and Technology (DGIST), 333 Techno Jungang-daero, Hyeonpung-eup, Dalseong-gun, Daegu 42988, Republic of Korea

E-mail: yongmin.ko@dgist.ac.kr

[§]These authors equally contribute this work.

Experimental Section

Materials: Poly(dimethylsiloxane) (Sylgard 184) was obtained from Dow Corning. Gold(III) chloride trihydrate ($HAuCl_4 \cdot 3H_2O$), sodium borohydride ($NaBH_4$), polystyrene (PS) microparticles, tetraoctylammonium bromide (TOABr), and tris(2-aminoethyl)amine (TREN) were purchased from Sigma-Aldrich. The PS microparticles were vacuum-dried to obtain a fine powder prior to use. All reagents were utilized as received without any additional purification.

Synthesis of TOABr-Au NPs dispersed in toluene: Au NPs with an average diameter of ~7 nm were synthesized in toluene using a modified Brust–Schiffrin method.[S1] Briefly, an aqueous solution of gold(III) chloride (30 mM, 30 mL) was mixed with a toluene solution of tetraoctylammonium bromide (25 mM, 80 mL) under vigorous stirring to promote phase transfer of the Au precursor into the organic phase. After 40 min, the aqueous layer was removed, and an aqueous $NaBH_4$ solution (0.4 M, 25 mL) was added to initiate reduction. The reaction mixture was stirred for 2.5 h, after which the toluene phase containing the Au NPs was collected and sequentially washed with 0.1 M H_2SO_4, deionized water (twice), 0.1 M NaOH, and deionized water (twice).

Preparation of 200 μm-thick flat/concave PDMS substrates: A flat PDMS film was prepared as follows. The PDMS precursor and curing agent were thoroughly mixed at a 10:1 (w/w) ratio and degassed by centrifugation at 3000 rpm for 3 min. The resulting prepolymer mixture was spin-coated onto a glass slide at 400 rpm for 30 s and subsequently cured at 100 °C for 1 h. After curing, the flat PDMS film was carefully peeled from the glass substrate. The concave PDMS film was fabricated using a colloidal templating approach. A PDMS prepolymer mixture was first spin-coated onto a glass substrate at 1000 rpm for 30 s and cured at 100 °C for 1 h. After curing, polystyrene (PS) microparticles were distributed onto the PDMS-coated glass by gently rubbing with another PDMS sheet, and excess particles were removed using an air gun.

This manual rubbing process enabled the self-assembly of PS microspheres into a hexagonally ordered colloidal monolayer. Although automated pressure control or quantitative monitoring was not employed due to the manual nature of the process, the formation of a uniform array was verified by SEM imaging. Subsequently, the PS-coated glass substrate was placed on a leveled surface, and fresh PDMS prepolymer was poured over the PS array. The sample was kept under vacuum for 2 h to remove trapped air between the PS spheres and then cured at 100 °C for 1 h. After curing, the concave PDMS layer was carefully detached from the PS template. Residual PS particles were removed by repeated pressing and peeling with adhesive tape, followed by sonication in acetone at 50 °C overnight.

Preparation of TREN/C-Ni-PDMS: The concave PDMS substrate was first thiol-functionalized following the method reported by Brook *et al.* [S2] to create a surface with high metal affinity. Briefly, the embossed PDMS film was sonicated at 50 °C for 6 h in a solution containing 1.23 mL of (3-mercaptopropyl)trimethoxysilane and 13 mL of a 1 wt% KOH-methanol solution. The resulting thiolated PDMS (SH-PDMS) was thoroughly washed with fresh methanol and subsequently soaked in dichloromethane (DCM) to remove unreacted silane species. To prepare the nickel-electroplated PDMS electrode, a conductive seed layer was first deposited onto the SH-PDMS substrate via a ligand-exchange-mediated layer-by-layer (LbL) assembly process, followed by Ni electroplating. The conductive seed layer was formed by alternately depositing TOABr-stabilized Au NPs (5 mg mL^{-1} in toluene) and TREN (1 mg mL^{-1} in ethanol) onto the SH-PDMS substrate. Specifically, the SH-PDMS was immersed in the TOABr-Au NP solution for 30 min and then rinsed with pure toluene to remove weakly bound Au NPs. The Au NP-coated substrate was subsequently immersed in the TREN-dissolved ethanol solution (TREN concentration ~1 mg mL^{-1}) for 15 min and rinsed with pure ethanol. This deposition cycle was repeated until sufficient surface conductivity was achieved for subsequent Ni electroplating. The resulting (Au NP/TREN)$_n$-coated PDMS substrate was electroplated in a conventional Watts bath containing 240 g L^{-1} $NiSO_4$, 45 g L^{-1} $NiCl_2$, and 30 g L^{-1} H_3BO_3. Ni electroplating was conducted using a two-electrode configuration, with the PDMS substrate serving as the cathode and a Ni plate as the anode, separated by a fixed distance of 2.5 cm. A current density of 25 mA cm^{-2} was applied, after which the sample was rinsed with deionized water and dried under vacuum. Finally, the C-Ni-PDMS sample was immersed in a TREN solution (1 mg mL^{-1}) for 15 min, rinsed with ethanol, and dried in a vacuum chamber.

Computational details: Spin-polarized density functional theory (DFT) calculations were performed using Vienna Ab initio Simulation Package (VASP, version 5.4.4).[S3,S4] The projected augmented wave (PAW) pseudopotential method and Perdew-Burke-Ernzerhof (PBE) exchange-correlation functional with Grimme's DFT-D3 scheme were used.[S5-S8] The cutoff energy was set to 400 eV. The adsorption energy calculations were carried out using a (2×2×1) Monkhorst-Pack k-points mesh.[S9] A vacuum region of 20 Å was implemented in the z-direction to avoid interactions between repeating images. The convergence criteria were set to 10^{-4} eV for energy and 0.05 eV/Å for force. For the electronic structure calculations, we used the GGA+U approach by Dudarev et al.[S10] The U correction value was chosen as 6.2 eV for Ni[S11]. The bulk structure of $Ni(OH)_2$ was constructed using (4×4×2) supercell. TREN/$Ni(OH)_2$ slab was modeled by incorporating a TREN (Tris(2-aminoethyl)amine) molecule onto the $Ni(OH)_2$ surface.

The adsorption energies (E_{ad}) of Li^+, NO_3^- and $TFSI^-$ anions, DME and DOL solvent molecules were calculated by the following equation[S12]

$$\Delta E_{ad} = E_{Total} - E_{Slab} - E_{Adsorbate}$$

Where E_{total}, E_{slab} and $E_{adsorbate}$ are the DFT energies of the total adsorbed system, the bare slab (i.e., $Ni(OH)_2$,TREN/$Ni(OH)_2$) and the isolated molecules in the (20 × 20 × 20) $Å^3$ cell, respectively. The charge density difference (Δρ) was calculated using the equation below

$$\Delta\rho = \rho_{\mathrm{Total}} - \rho_{\mathrm{Slab}} - \rho_{\mathrm{Adsorbate}}$$

in which ρ_{Total}, ρ_{Slab} and $\rho_{\mathrm{Adsorbate}}$ correspond to the charge density values for the total system, the slab and the adsorbate molecule, respectively.

To evaluate solvation effects, an implicit solvation model was employed using the VASPsol.[S13, S14] The solvent dielectric constant was set to 7.17 to simulate DME/DOL (1:1, v/v) [S15] and 1 M $LiPF_6$ dissolved in EC/DEC (1:1, v/v) with 10 wt% FEC [S16], respectively. The Debye length was set to 3.04 Å to simulate a 1 M condition.

Electrochemical simulation: To investigate how the geometry of the microcavities influences Li-ion transport and electrochemical response, numerical simulations were carried out using COMSOL Multiphysics 6.3. The Tertiary Current Distribution with electroneutrality was employed under stationary conditions with an initialization step. All physicochemical parameters—including the diffusion coefficients of Li^+ and $TFSI^-$, reference exchange current density, ionic conductivity, transference number, and viscosity—were taken from literature values corresponding to 1 M LiTFSI in a 1:1 (v/v) mixture of 1,3-dioxolane (DOL) and dimethoxyethane (DME).[S17-S19]

Since charge transport in the electrolyte occurs via ionic motion, the electrolyte current density was expressed as the sum of the ionic fluxes:

$$\mathrm{i_l} = F \sum z_i \, \mathrm{N_i}$$

where i_l is the electrolyte current density (A m^{-2}), F is the Faraday constant (96 485 C mol^{-1}), N_i is the flux of species i, and z_i is its charge number.

Cell Assembly and Electrochemical Measurements: Electrochemical measurements were conducted using CR2032-type coin cells (MTI Corporation) and a WBCS3000 multichannel workstation. All cells were assembled in an argon-filled glovebox (MBraun; $O_2 < 0.1$ ppm, H_2O

< 0.1 ppm. For Li‖C-Ni-PDMS and Li‖TREN/C-Ni-PDMS half-cells, as well as Li-TREN/C-Ni-PDMS symmetric cells, lithium metal foil (35 μm thick) was used as the counter/reference electrode, the as-prepared electrodes served as the working electrodes, and a glass-fiber separator (750 μm thickness) was employed. The electrolyte consisted of 1 M LiTFSI dissolved in 1,2-dimethoxyethane (DME)/1,3-dioxolane (DOL) (1:1, v/v) with 5 wt% $LiNO_3$ as an additive. Prior to full-cell assembly, Li was electrodeposited onto the C-Ni-PDMS or TREN/C-Ni-PDMS electrodes in a half-cell configuration, using Li metal foil as both the counder and reference electrode and an electrolyte of 1 M LiTFSI in DME/DOL (1:1 v/v) with 5 wt% $LiNO_3$ at 0.5 mA cm^{-2} for 20 h (10 mAh cm^{-2}). No additional post-treatment was applied after Li deposition before full-cell preparation. The pre-lithiated electrode was then retrieved and assembled with an LFP cathode. For Li‖LFP full cells, the electrolyte consisted of 1 M $LiPF_6$ dissolved in ethylene carbonate (EC)/diethyl carbonate (DEC) (1:1, v/v), supplemented with 10 wt% fluoroethylene carbonate (FEC). Li-C-Ni-PDMS or Li-TREN/C-Ni-PDMS anodes (with a Li areal capacity of 10 mAh cm^{-2}) were paired with LFP cathodes prepared by slurry casting onto Al foil (Sigma-Aldrich), with an active material loading of 7.8 mg cm^{-2}. The cathode slurry consisted of active material, conductive carbon, and binder in a weight ratio of 8.8:0.4:0.8, resulting in a cathode thickness of approximately 83 μm. A glass-fiber separator (750 μm thickness) was used in all full cells. In all coin cells, the electrolyte volume was fixed at 100 μL. GCD tests for Li-TREN/C-Ni-PDMS‖LFP full cells were performed within a voltage window of 2.5–3.9 V under comparable testing conditions. GCD tests for Li-TREN/C-Ni-PDMS‖LFP full cells were performed within a voltage window of 2.5–3.9 V under comparable testing conditions. The theoretical capacity of LFP used for C-rate calculations was 170 mAh g^{-1}. Electrochemical impedance spectroscopy (EIS) measurements were carried out over a frequency range from 100 kHz to 0.1 Hz with a perturbation amplitude of 0.01 mV. All electrochemical measurements were conducted at room temperature (25 °C). Diffusion coefficient (*D)* can significantly affect Li-ion transport, interfacial resistance, and overall

battery performance. Based on the parameters obtained from the Nyquist plots after 10 galvanostatic cycles, the *D* for each cell were calculated using the following equations:

$$Z' = R_s + R_{ct} + \sigma_w \omega^{-0.5} \tag{1}$$

$$D = 0.5 \left(\frac{RT}{AF^2 \sigma_w C}\right)^2 \tag{2}$$

where σ_w is the Warburg impedance coefficient, ω is the angular frequency, R is the gas constant, T is the absolute temperature (K), A is the electrode area (cm^2), F is Faraday's constant ($C\ mol^{-1}$), and C is the molar concentration of ions in the electrolyte ($mol\ L^{-1}$).

Pouch cell assembly. Pouch cells were assembled in an argon-filled glovebox (MBraun; $O_2 <$ 0.1 ppm, $H_2O <$ 0.1 ppm). Prior to full-cell assembly, Li was electrodeposited onto the TREN/C-Ni-PDMS electrode at a current density of 0.5 mA cm^{-2} for 20 h, corresponding to a plating capacity of 10 mAh cm^{-2}, using an electrolyte consisting of 1 M LiTFSI dissolved in 1,2-dimethoxyethane (DME)/1,3-dioxolane (DOL) (1:1, v/v) with 5 wt% $LiNO_3$. The pre-plated electrode was subsequently retrieved and employed as the anode in the pouch-type full cell. For pouch cell fabrication, aluminum and nickel tabs were attached to the cathode and anode, respectively, via ultrasonic welding (GN-800, Gelon). The cell was then assembled by sequentially stacking a 20 μm-thick Li-coated Cu foil (Cu foil thickness: 11 μm), separator, the Li-TREN/C-Ni-PDMS anode, and a $LiFePO_4$ cathode with an areal loading of 17.1 mg cm^{-2} (~2.9 mAh cm^{-2}) within a laminated pouch. The full cell was assembled using an electrolyte consisting of 1 M $LiPF_6$, in ethylene carbonate (EC)/diethyl carbonate (DEC) (1:1, v/v), supplemented with 10 wt% fluoroethylene carbonate (FEC) and after electrolyte injection, the pouch cell was vacuum-sealed to complete the assembly.

Charaterization: The size and morphology of the TOABr-Au nanoparticles were examined by high-resolution transmission electron microscopy (HR-TEM; Tecnai F20, FEI). Fouriertransform infrared (FTIR) spectra of the (TOABr-Au NP/TREN)$_n$ multilayer films deposited on SH-treated Si wafers were recorded using a Cary 600 spectrometer (Agilent Technologies) in advanced grazing-angle (AGA) mode with a resolution of 4 cm^{-1}. The FTIR spectra were baseline-corrected and analyzed using spectral analysis software (OMNIC, Thermo Fisher Scientific). The mass change (Δm, μg cm^{-2}) of the (Au NP/TREN)$_n$ multilayer films deposited on quartz crystal microbalance (QCM) electrodes was determined from the corresponding frequency shifts ($-\Delta$F, kHz) measured using a QCM 200 system (Stanford Research Systems). The mass change was calculated based on the simplified Sauerbrey equation: $-\Delta F = 56.6 \times \Delta m$. The surface and cross-sectional morphologies of the PDMS-based electrodes, along with elemental mapping, were characterized using field-emission scanning electron microscopy (FE-SEM; Hitachi S-4800) equipped with energy-dispersive X-ray spectroscopy (EDS) and atomic force microscopy (AFM; XE-100, Park Systems) operated in non-contact mode. UV-vis absorption spectra of the multilayer films deposited on quartz substrates were collected using a Lambda 35 spectrophotometer (PerkinElmer) over a wavelength range of 200–800 nm. The sheet resistance of the electrodes was measured using a four-point probe system (MCP-T610, Mitsubishi Chemical Analytech). Changes in electrical resistance under mechanical deformation were monitored using a two-point probe configuration with a Keithley 4200-SCS semiconductor characterization system. Electrolyte contact angles were determined via a sessile drop method using a Phoenix-300 goniometer (SEO Corp.). Nanoindentation measurements were performed to evaluate the effective elastic modulus of the metallized elastomer electrodes. The tests were conducted using a nanoindenter system (NanoTest Vantage Platform, Micro Materials, UK) equipped with a Berkovich diamond indenter. Prior to testing, the instrument was calibrated using a fused silica standard following the Oliver–Pharr procedure. All measurements were carried out in load-controlled mode. The maximum indentation depth was fixed at approximately 6 μm to ensure that the indentation response reflected the mechanical properties of the metallized elastomer composite rather than only the surface Ni layer. A loading-holding-unloading sequence was applied, consisting of a 10 s loading segment, a 5 s holding period at the peak load to minimize viscoelastic creep effects, and a 10 s unloading segment. For each sample, at least 5 indents were recorded at randomly selected positions to obtain statistically reliable values. The reduced modulus (E_r) was extracted from the unloading stiffness of the load-displacement curves using the Oliver-Pharr analysis. The elastic modulus (E_s) of the elastomer-supported hybrid electrode was calculated from the conventional relation between E_r and E_s, assuming negligible compliance of the diamond indenter and a Poisson's ratio of 0.50 for the elastomer substrate.

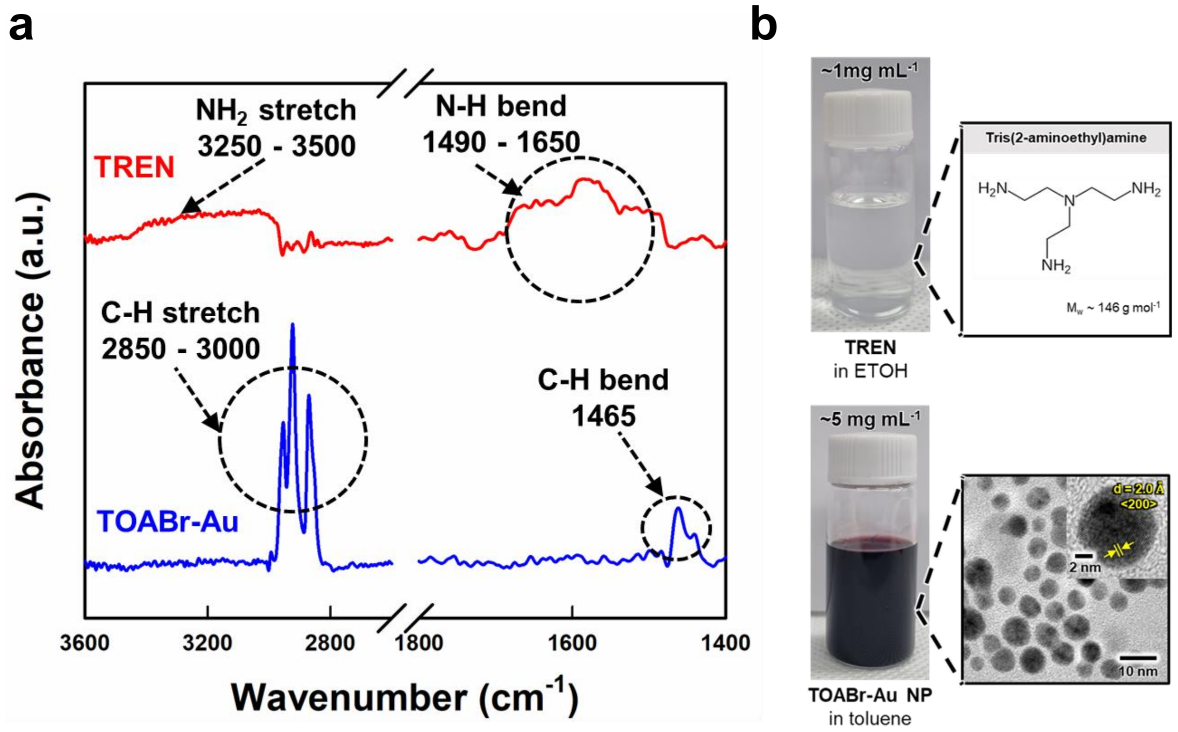

Figure S1. a) FTIR spectra of TOABr-Au NPs and TREN molecule, and b) digital images of TOABr-Au NPs dispersed in toluene and TREN dissolved in ethanol. The expanded images of b) present the chemical structure of TREN (top) and the HR-TEM image (bottom) of TOABr-Au NPs, respectively. The TOABr-Au NPs exhibit strong vibrational bands in the regions of 2850–2960 cm^{-1} and at 1465 cm^{-1}, which are attributed to the long aliphatic chains of the TOABr ligands. Additionally, TREN displays characteristic peaks in the ranges of 3250–3500 cm^{-1} and 1490–1650 cm^{-1}, corresponding to the stretching and bending vibrations of NH$_2$ groups.

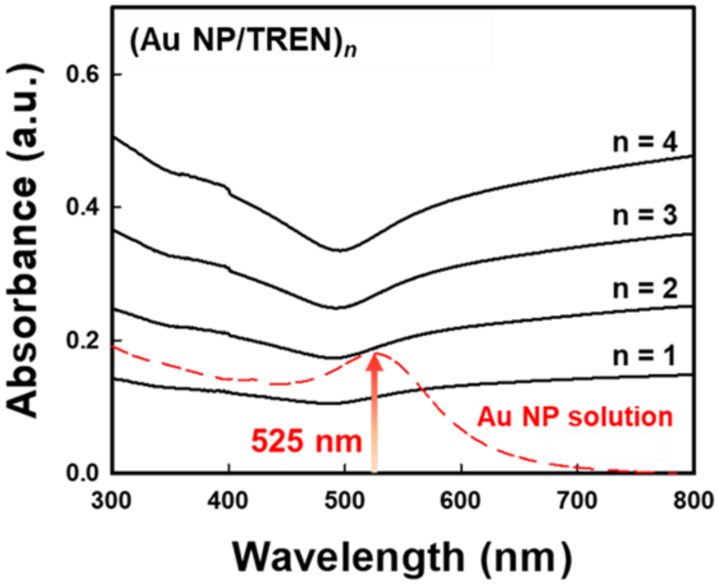

Figure S2. UV-vis spectra of (Au NP/TREN)$_n$ multilayers as a function of bilayer number (*n*). As the bilayer number (*n*) increases, the surface plasmon resonance peak of the Au NPs progressively red-shifts toward the near-infrared (IR) region. This red shift indicates a significant reduction in the interparticle spacing between adjacent Au NPs, resulting in the formation of a densely interconnected metallic network.

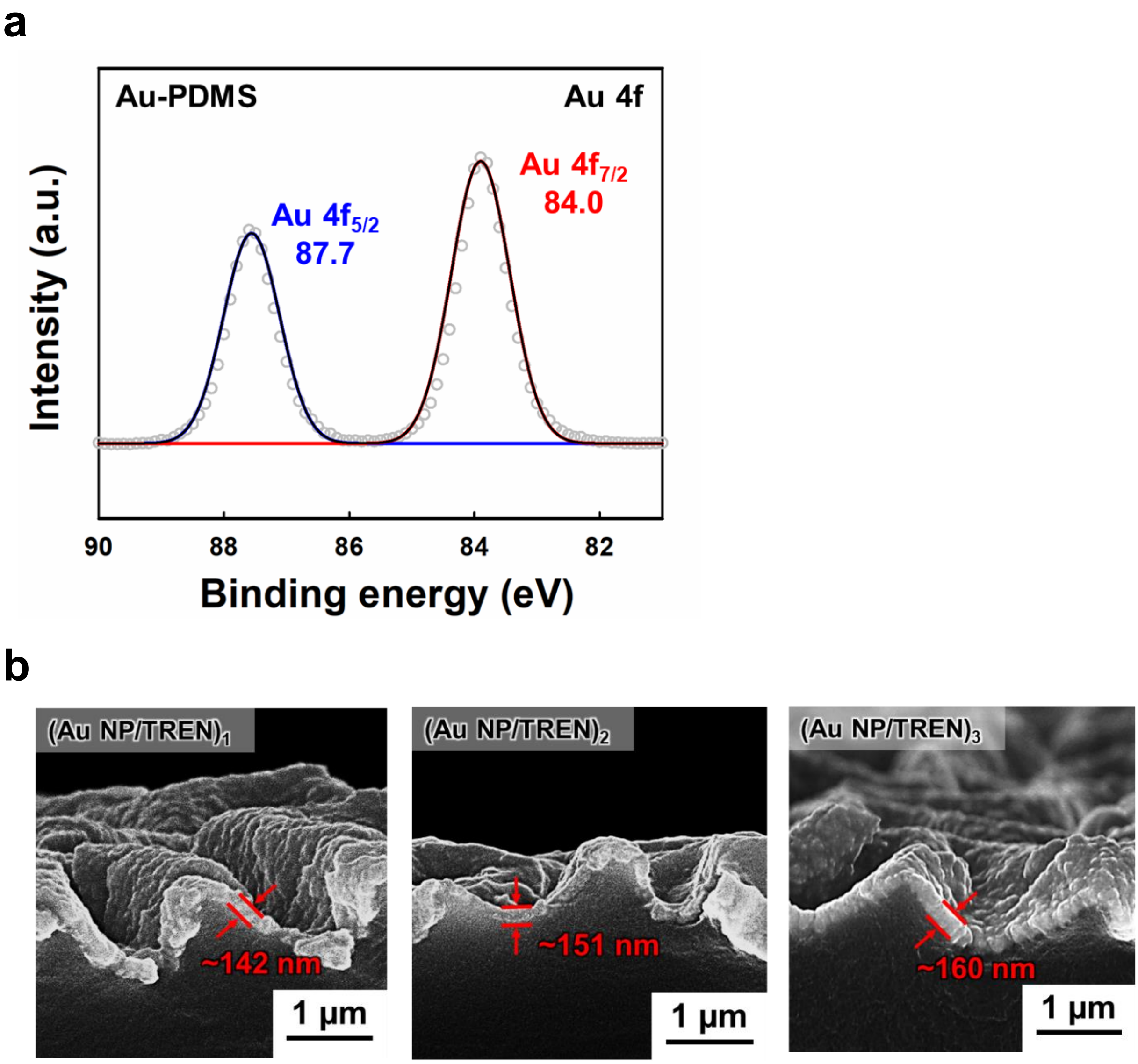

Figure S3. a) High-resolution Au 4f XPS spectrum of (Au NP/TREN)$_3$-coated PDMS (Ni-PDMS). The spectrum exhibits two characteristic peaks at 84.0 eV (Au 4f$_{7/2}$) and 87.7 eV (Au 4f$_{5/2}$), which correspond to the spin-orbit doublet of metallic Au^0, evidencing the metallic character of the LbL-assembled Au NP network arising from their closely packed arrangement. b) Cross-sectional FE-SEM images of (Au NP/TREN)$_{n=1,2,3}$ multilayers deposited on PDMS, showing sequential increases in film thickness (~142 nm for $n = 1$, ~151 nm for $n = 2$, and ~160 nm for $n = 3$, respectively) as the bilayer numbers increases.

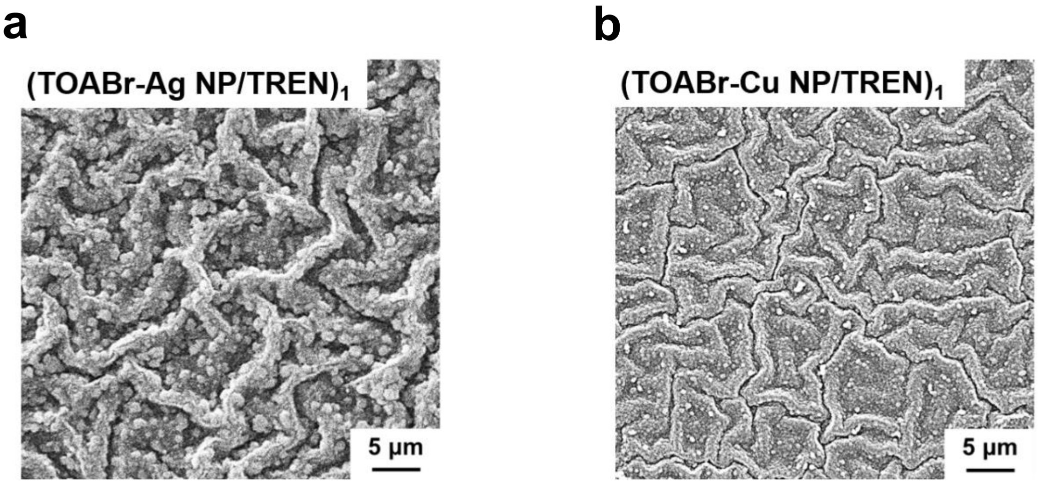

Figure S4. a) FE-SEM images of (TOABr-Ag NP/TREN)$_1$ and b) (TOABr-Cu NP/TREN)$_1$-coated PDMS substrates showing the successful formation of crumple and interconnected NP networks.

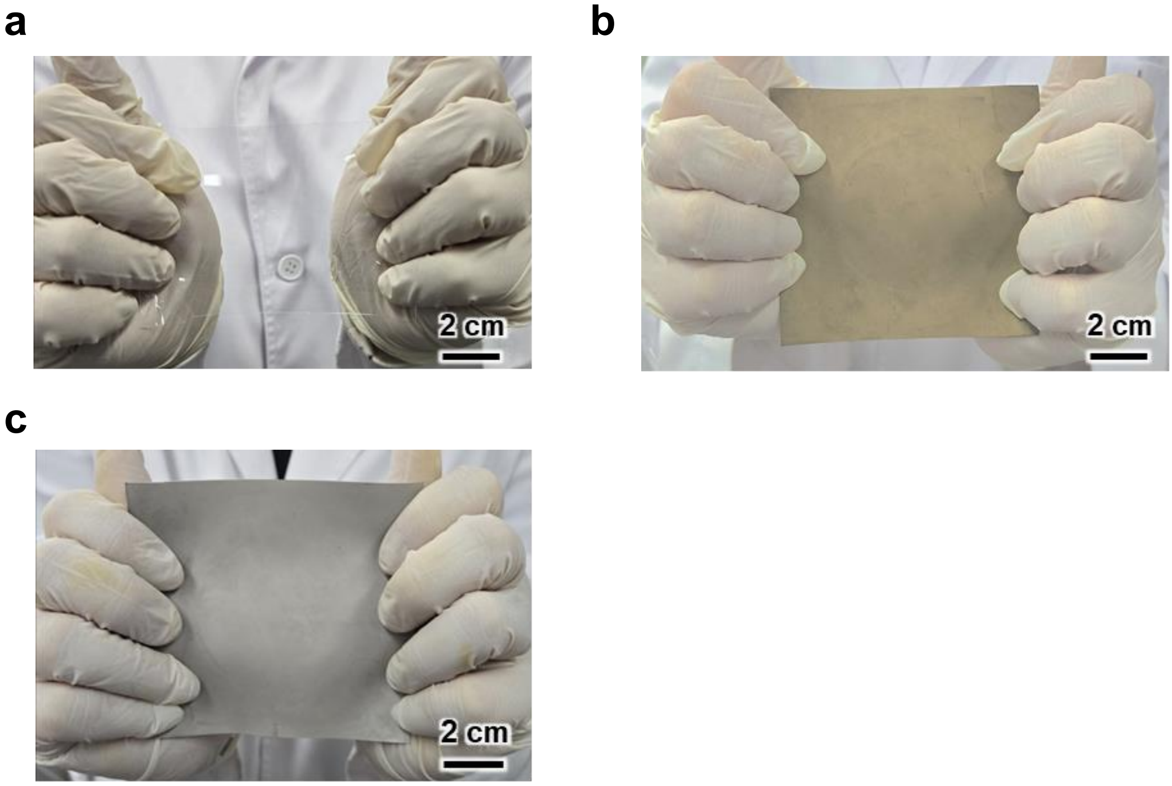

Figure S5. Photographic images of a) bare PDMS elastomer, b) (TOABr-Au NP/TREN)$_1$-coated nanocrumpling PDMS elastomer, and c) F-Ni-PDMS. The size of PDMS substrate is 10 cm × 10 cm.

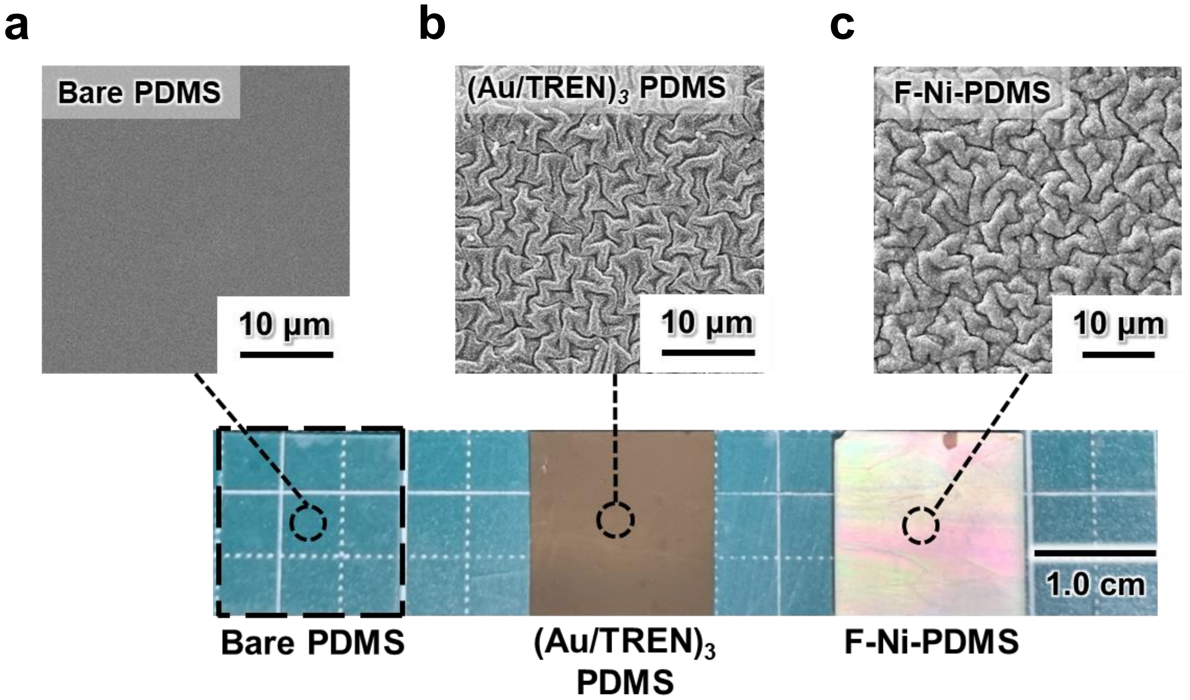

Figure S6. Digital photopraphs and corresponding top-view FE-SEM imgase of a) bare PDMS, b) (Au NP/TREN)$_3$ multilayer-coated PDMS, and c) F-Ni-PDMS.

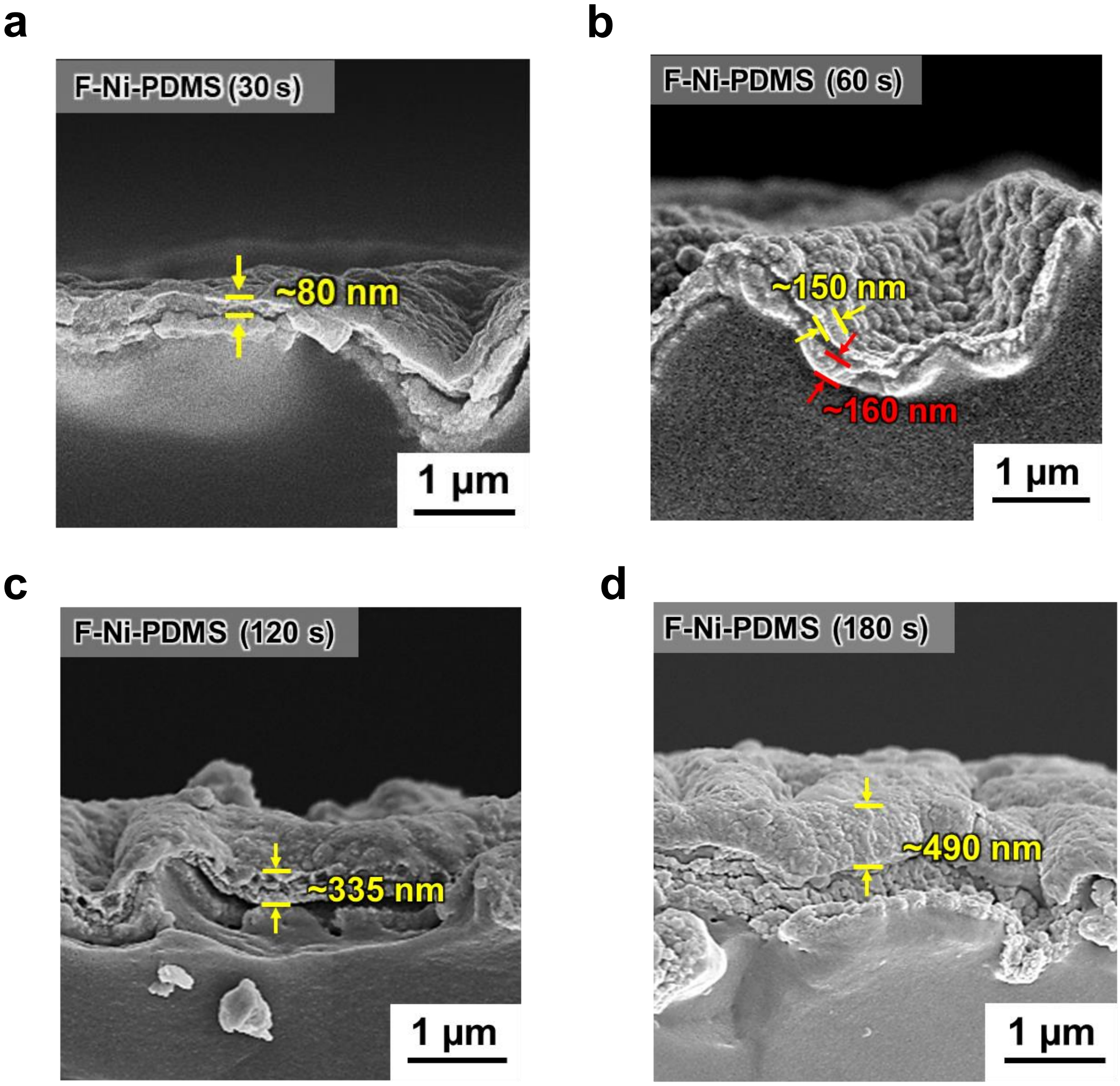

Figure S7. Cross-sectional FE-SEM images of PDMS hosts after deposition of (Au NP/TREN)$_3$ multilayers and after subsequent Ni electroplating for a) 30 s, b) 60 s, c) 120 s, and d) 180 s. The results confirm the uniform and well-defined growth of each deposited layer.

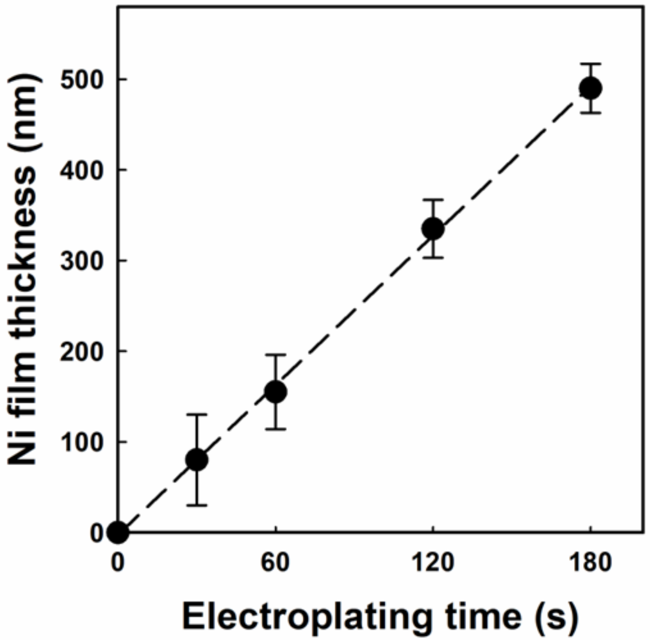

Figure S8. Ni film thickness as a function of electroplating time was obtained from cross-sectional FE-SEM images of **Figure S5**. The measured thicknesses (~80 nm at 30 s, ~150 nm at 60 s, ~335 nm at 120 s, and ~490 nm at 180 s) exhibit a nearly linear time-dependent growth behavior, confirming the uniform and well-regulated deposition of Ni on the (Au NP/TREN)$_3$-assembled PDMS surface.

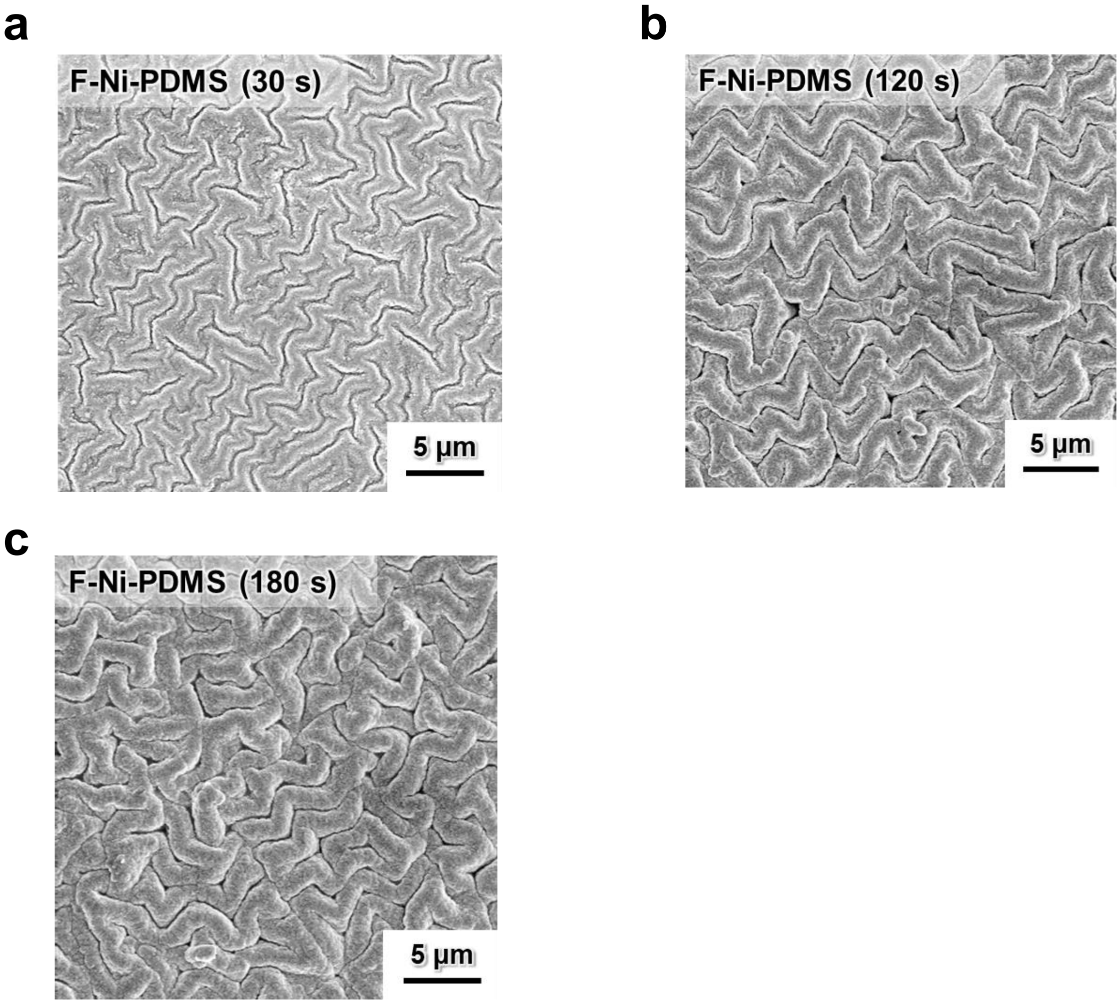

Figure S9. Top-view FE-SEM images of F-Ni-PDMS electroplated for a) 30 s, b) 120 s and c) 180 s. The crumple topology is maintained over the given plating duration.

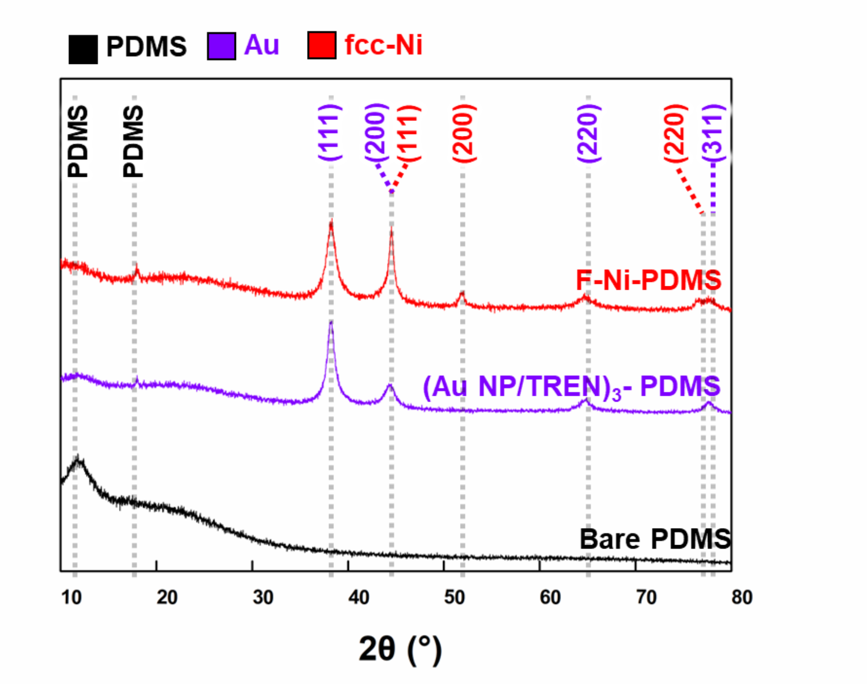

Figure S10. X-ray diffraction (XRD) patterns of bare PDMS, (Au NP/TREN)$_3$- PDMS, and F-Ni-PDMS. The Ni-PDMS sample shows distinct diffraction peaks at 44.6°, 52.0°, and 76.5°, corresponding to the (111), (200), and (220) planes of face-centered cubic (fcc) Ni, along with the peaks of Au. These results confirm the successful deposition of Au NPs (i.e., Au NP/TREN multilayers) onto the PDMS substrate, followed by subsequent Ni electroplating. The reference diffraction patterns for Au and fcc Ni correspond to JCPDS card numbers 04-0784 and 04-0850, respectively.

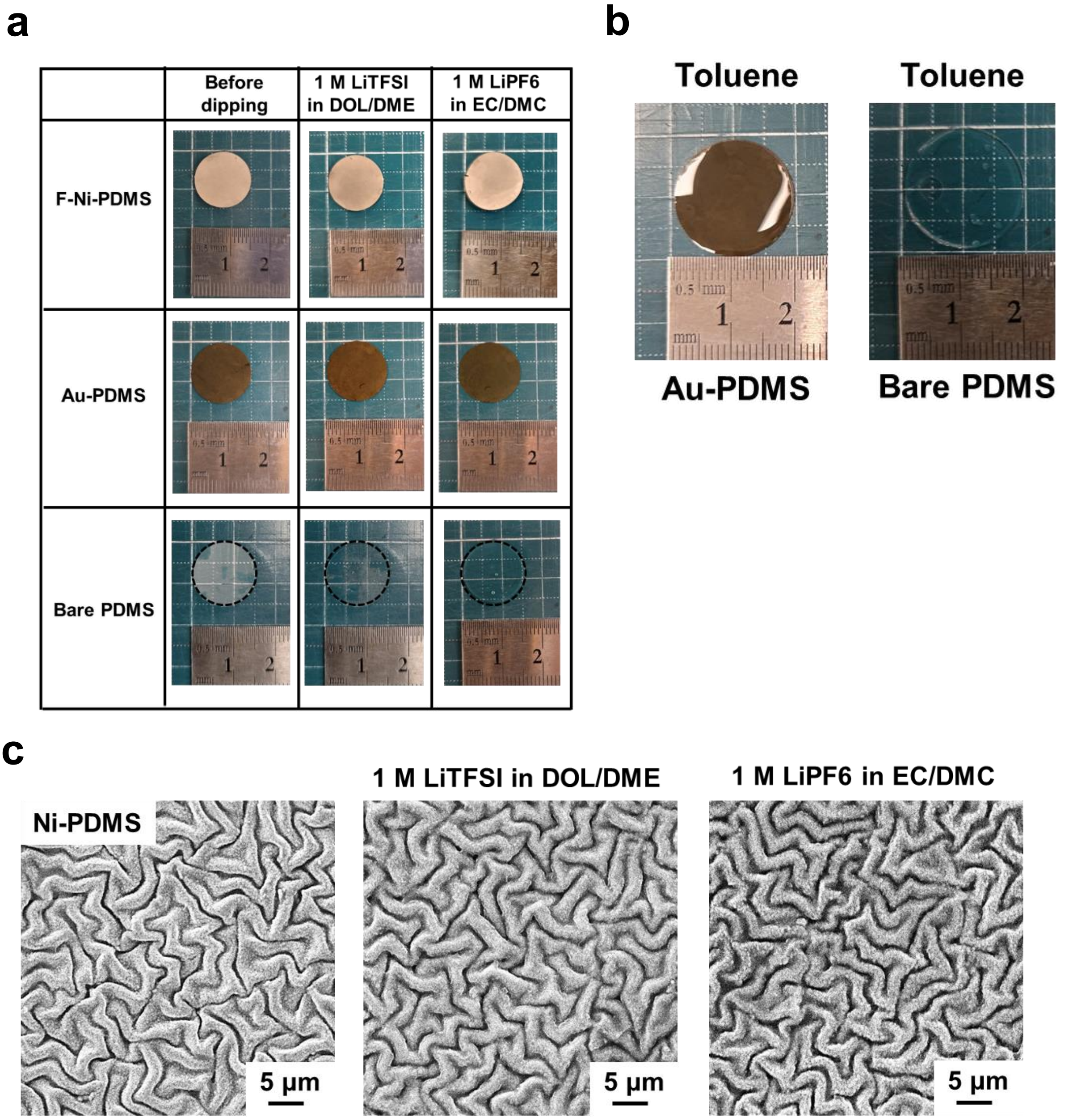

Figure S11. a) Digital images of bare PDMS, Au-PDMS, and Ni-PDMS after immersion in 1 M LiTFSI in DOL/DME and 1 M $LiPF_6$ in EC/DMC for 150 h, showing negligible dimensional change. b) Comparison of swelling behavior in toluene, demonstrating significantly larger expansion due to high solvent compatibility with PDMS. c) SEM images of Ni-PDMS before and after electrolyte immersion, confirming the preservation of the nano-crumpled structure without structural degradation.

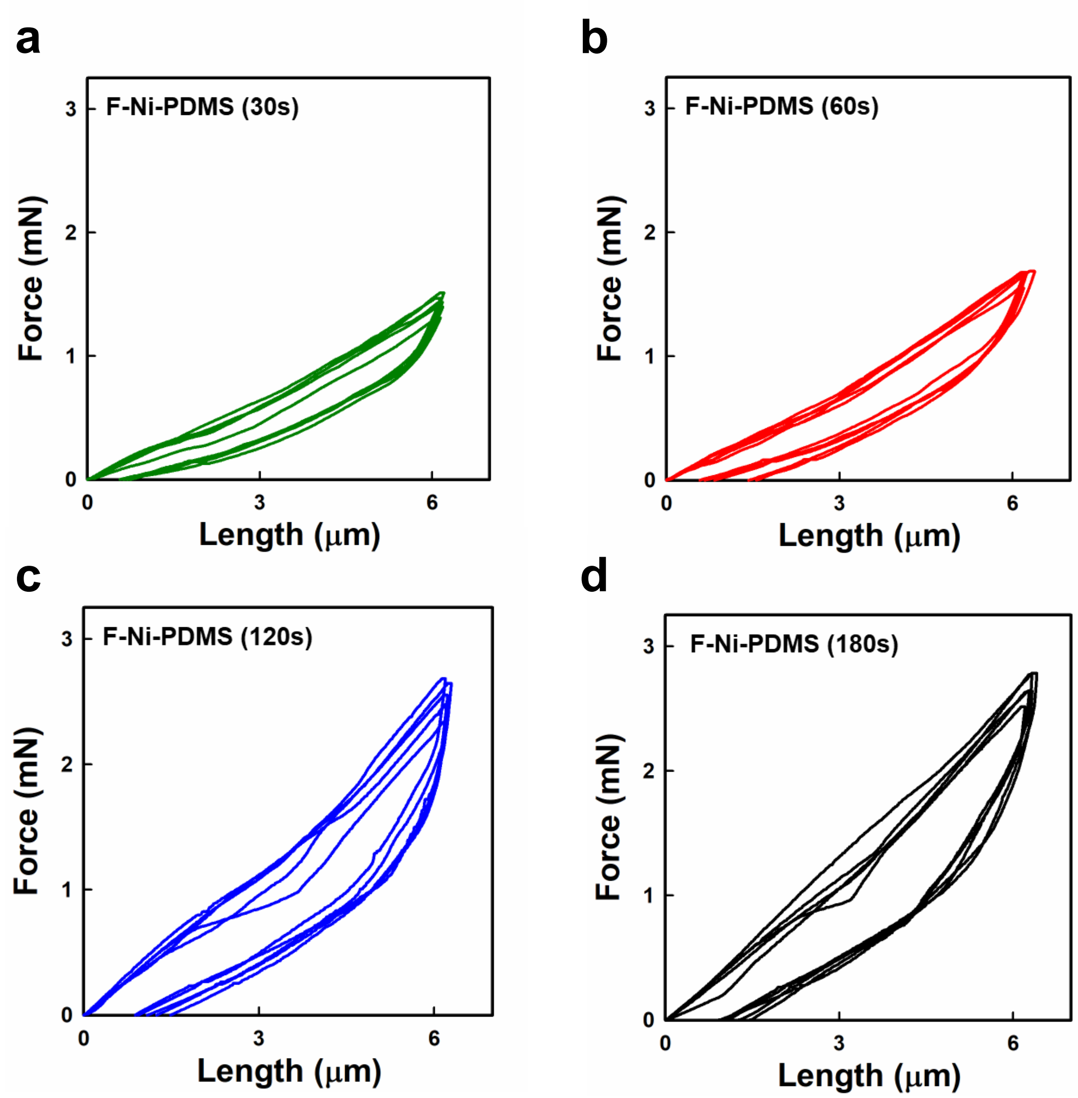

Figure S12. Load-displacement curves of F-Ni-PDMS electrodes with different Ni electroplating times: a) 30 s, b) 60 s, c) 120 s, and d) 180 s. Each panel displays representative loading-unloading cycles, demonstrating the reproducibility of the nanoindentation measurements. The 30 s and 60 s samples exhibit relatively lower loading stiffness and larger elastic recovery, indicative of a mechanically compliant metal-elastomer hybrid structure. By contrast, the 120 s and 180 s samples show noticeably steeper loading slopes and reduced elastic recovery, reflecting the increased stiffness arising from the thickened and densified Ni layer. The reduced modulus values were extracted from the unloading segments using the Oliver–Pharr method and subsequently converted into effective elastic moduli as described in the main text.

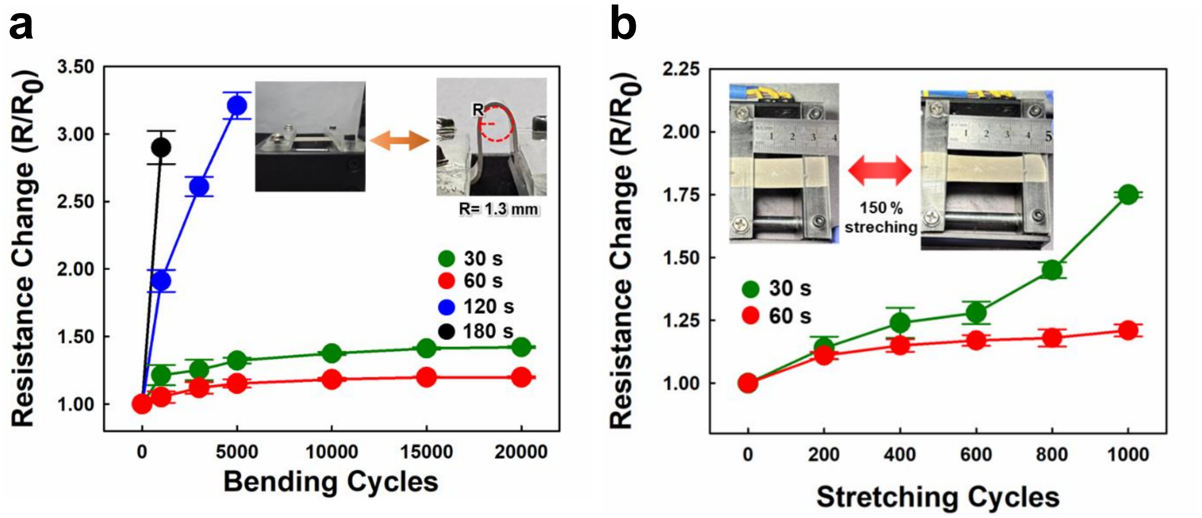

Figure S13. a) Resistance change (R/R₀) of F-Ni-PDMS electrodes with different Ni electroplating times during repeated bending at a bending radius of 1.3 mm. b) Resistance (R/R₀) of the electrodes during cyclic stretching to 150% strain.

.

cf

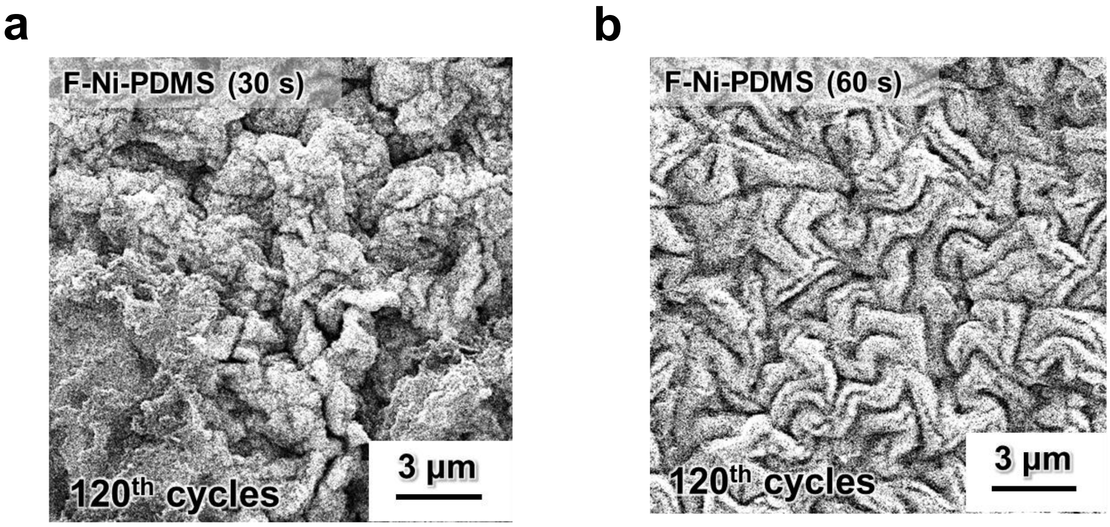

Figure S14. Top-view FE-SEM images of a) 30 s-electroplated and b) 60 s-electroplated F-Ni-PDMS electrodes after complete Li stripping to 1.0 V (vs. Li/Li$^+$) following 120 plating/stripping cycles at 1 mA cm^{-2} and 1 mAh cm^{-2}. The 30 s-electroplated electrode exhibits pronounced morphological disruption and fragmentation of the crumpled metallic framework, indicating progressive structural degradation during cycling. In contrast, the 60 s-electroplated electrode largely preserves its nano-crumpled architecture even after full Li removal, demonstrating superior mechanical robustness and interfacial stability under repeated cycling**.**

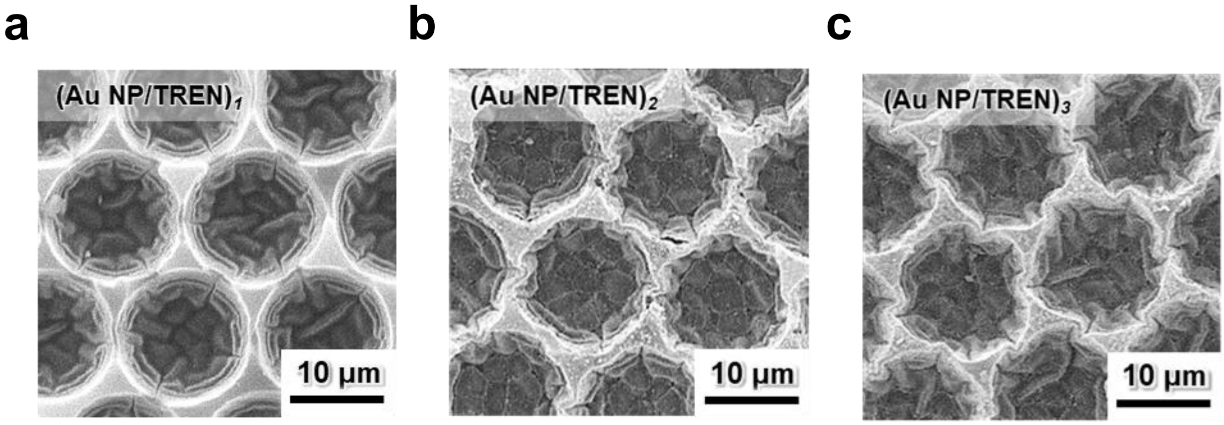

Figure S15. Top-view FE-SEM images of concave-structured PDMS substrate after the sequential deposition of a) (Au NP/TREN)$_1$, b) (Au NP/TREN)$_2$, and c) (Au NP/TREN)$_3$ multilayers.

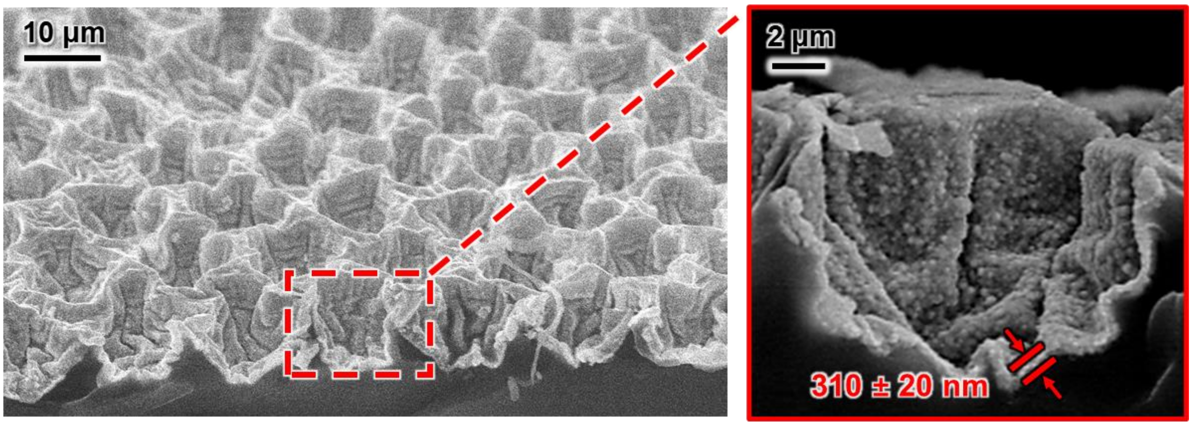

Figure S16. Cross-sectional FE-SEM images of C-Ni-PDMS. The low-magnification image (left) reveals the well-defined concave microstructures that are uniformly covered by the deposited Ni layer. The magnified cross-sectional image (right) further confirms that the crumple morphology is preserved even within the interior of the concave features and that Au NP and Ni film is uniformly deposited with a thickness of approximately 310 nm.

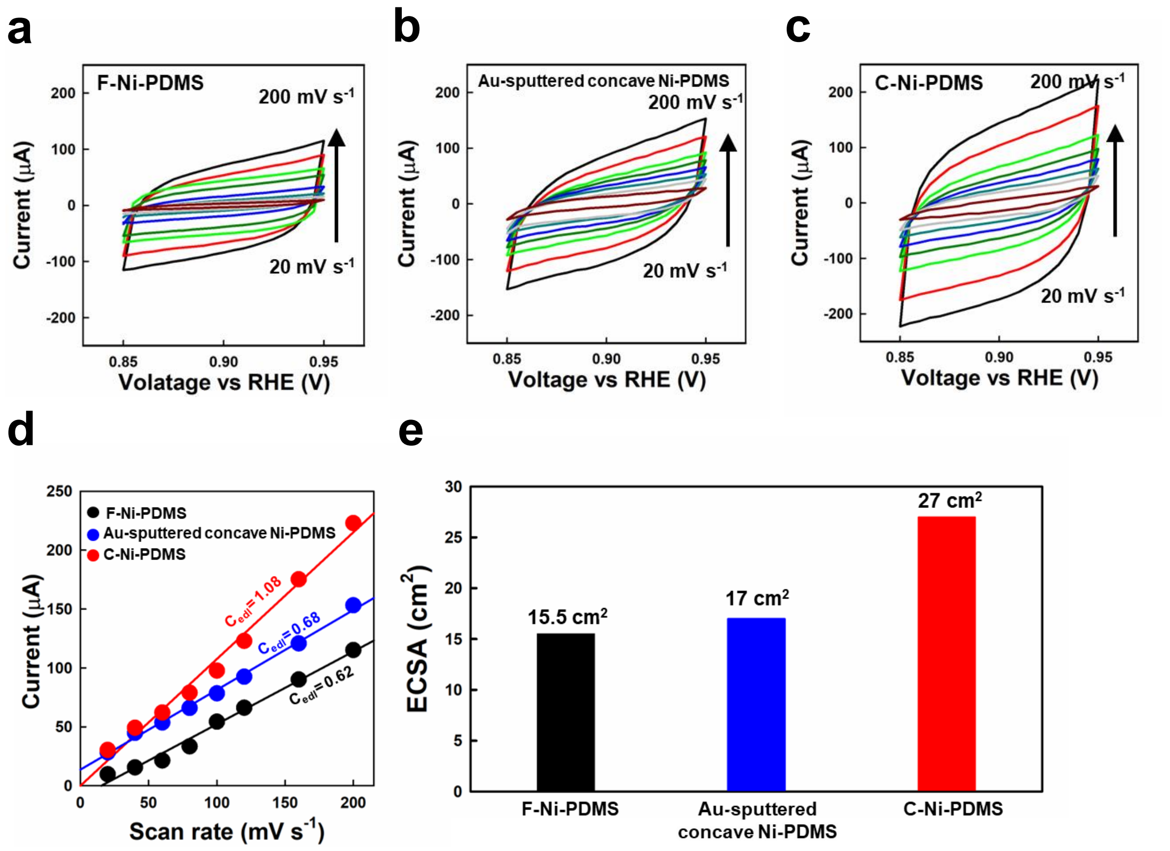

Figure S17. CV curves of a) F-Ni-PDMS, b) Au-sputtered concave Ni-PDMS and c) C-Ni-PDMS, recorded in the non-Faradaic potential window of 0.85–0.95 V at scan rates ranging from 20 to 200 mV s^{-1} in 1 M KOH aqueous solution. d) The capacitive current plotted as a function of scan rate for each electrode. The electric double-layer capacitance (C_{edl}) values were extracted as 0.62, 0.68, and 1.08 mF for F-Ni-PDMS, Au-sputtered concave Ni-PDMS, and C-Ni-PDMS, respectively. Notably, the crumpled C-Ni-PDMS exhibits a markedly higher C_{edl}, indicating a substantially increased electrochemically exposed surface area. e) Corresponding electrochemically active surface area (ECSA) values based on the relation ECSA = C_{edl}/C_s (C_s of Ni is 0.04 mF/cm^{-2}).[S20]

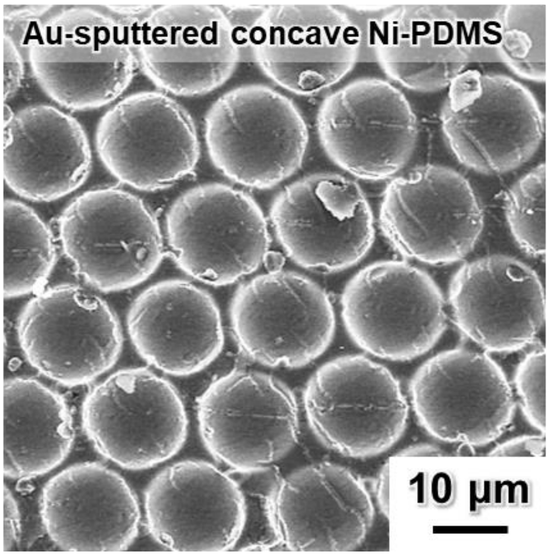

Figure S18. FE-SEM image of Au-sputtered concave Ni-PDMS. In this case, the cavity surfaces remain smooth without nanoscale crumples.

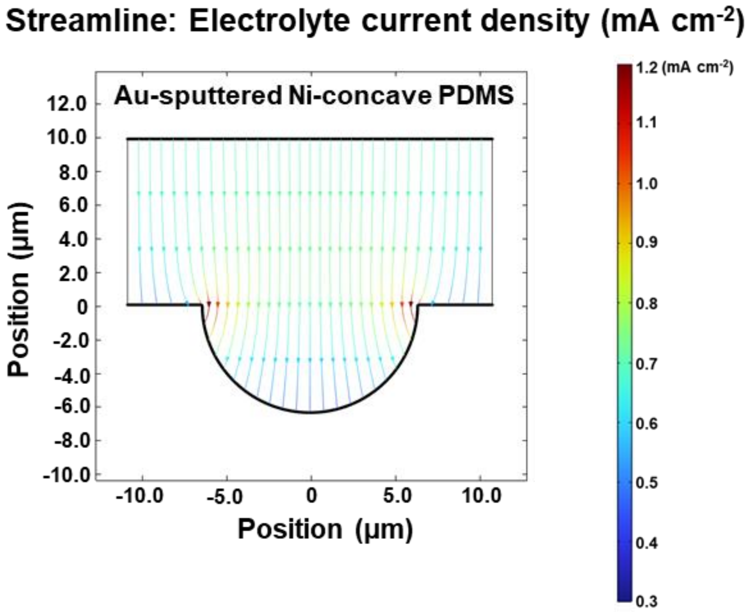

Figure S19. COMSOL Multiphysics simulation illustrating the electrolyte current density distribution within an Au-sputtered concave PDMS electrode. The current density is highly concentrated in the rim regions, whereas the recessed interior exhibits severely limited ionic access due to the absence of a crumpled architecture, highlighting the intrinsic limitations of smooth concave structures.

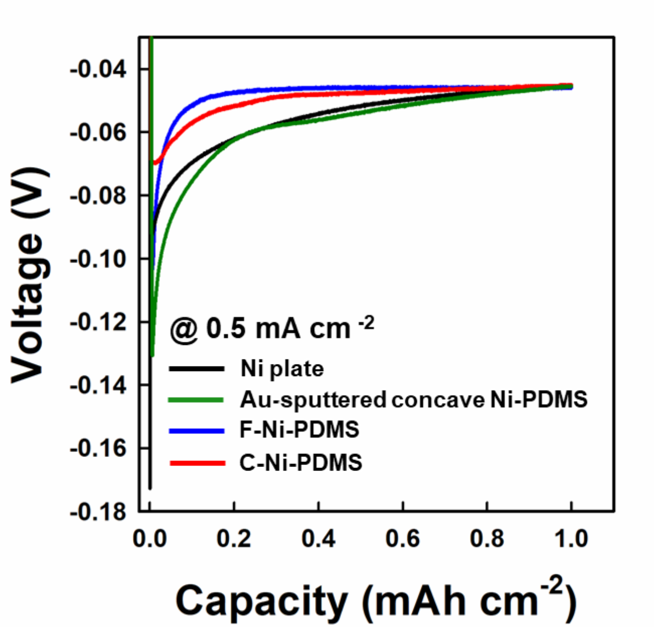

Figure S20. Voltage (V) *vs.* capacity (mAh cm^{-2}) profiles of half-cells based on a flat Ni plate, Au-sputtered concave Ni-PDMS, F-Ni-PDMS, and C-Ni-PDMS during Li nucleation at a current density 0.5 mA cm^{-2}.

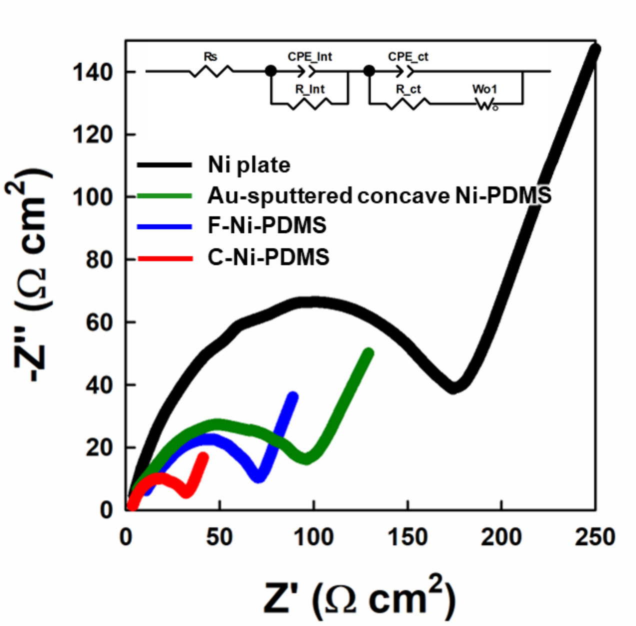

Figure S21. Nyquist plots of half-cells based on a flat Ni plate, Au-sputtered concave Ni-PDMS, F-Ni-PDMS, and C-Ni-PDMS electrodes.

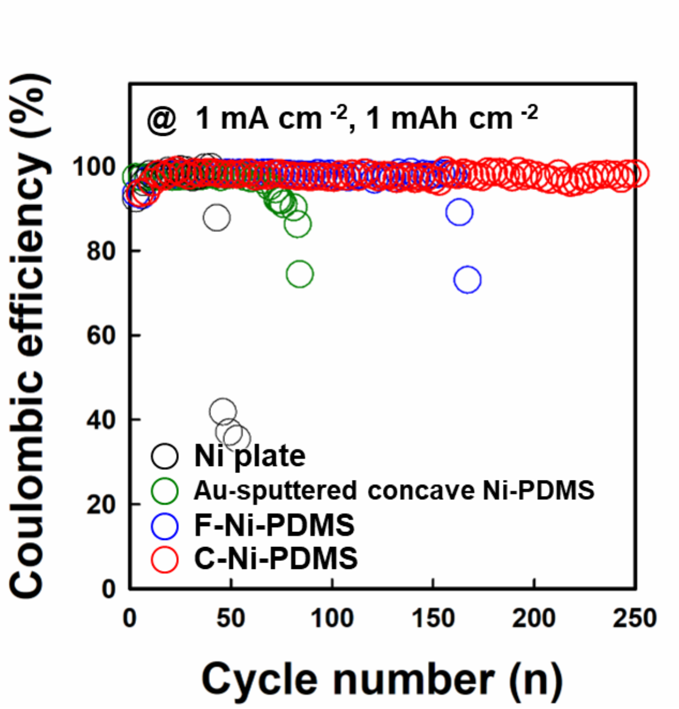

Figure S22. Trace of CE values of half-cells based on flat Ni plate, Au sputtered concave Ni-PDMS, F-Ni-PDMS, and C-Ni-PDMS electrodes during Li plating/stripping cycling at 1 mA cm^{-2} and 1 mAh cm^{-2}.

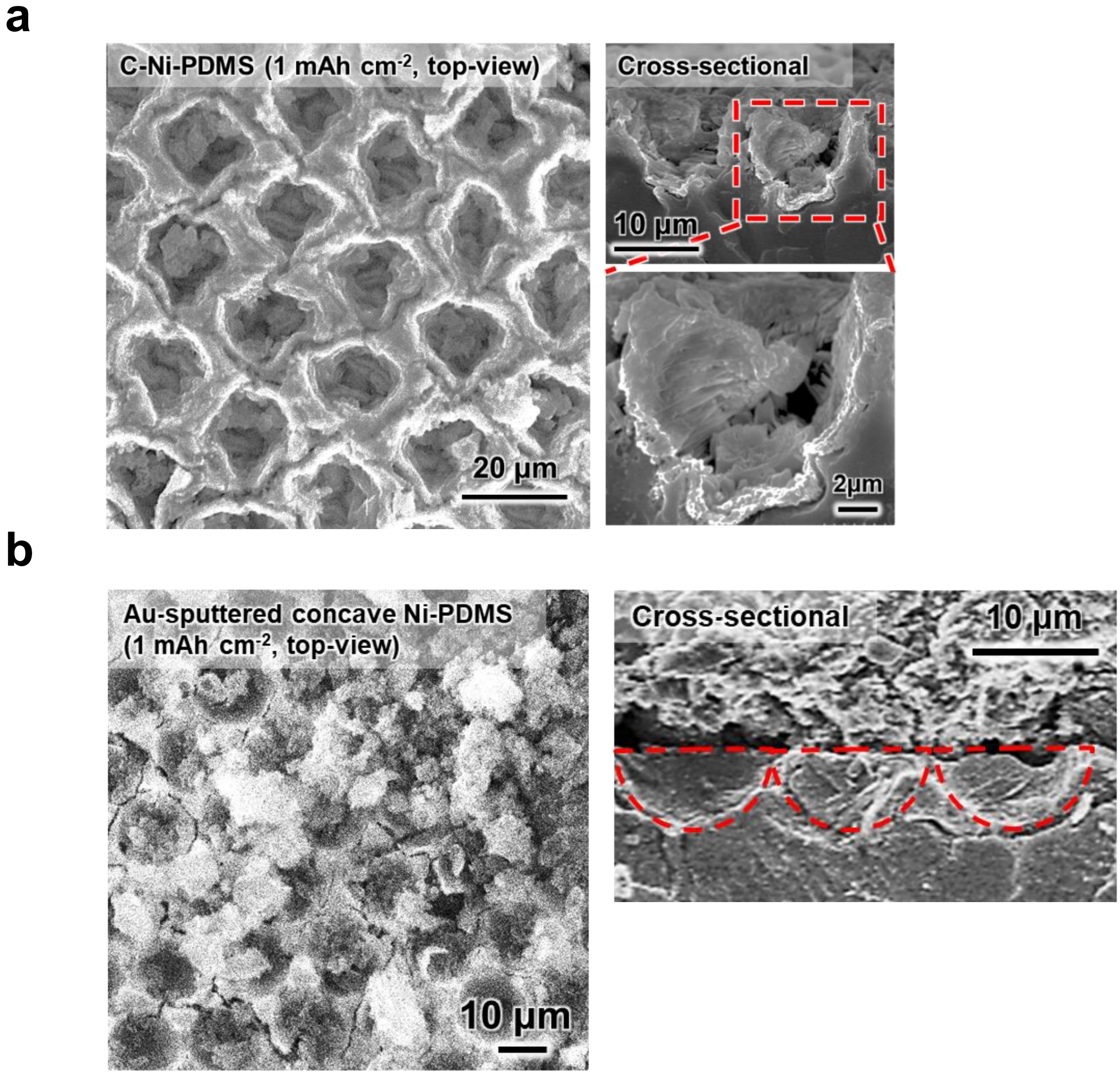

Figure S23. a) FE-SEM images of the C-Ni-PDMS electrode. The deposited Li forms a dense, conformal, and dendrite-free morphology that uniformly covers and fills the concave cavities. The magnified cross-sectional view further reveals layered Li growth along the crumpled interior surfaces, underscoring the effectiveness of the hierarchical crumpled-concave architecture in directing uniform Li deposition. b) FE-SEM images of the Au-sputtered concave Ni-PDMS electrode after plating 1 mAh cm^{-2} of Li at 0.5mA cm^{-2}. Top-view (left) and cross-sectional FE-SEM images (right) after plating 1 mAh cm^{-2} of Li at 0.5mA cm^{-2}. Highly non-uniform and porous Li deposition is observed predominantly near the rim regions, while the cavity interior remains sparsely filled. These observations are consistent with the simulation results (see **Figure S16**), confirming that smooth concave architectures, without nanoscale crumpling, are unable to facilitate uniform ionic accessibility or conformal Li accommodation.

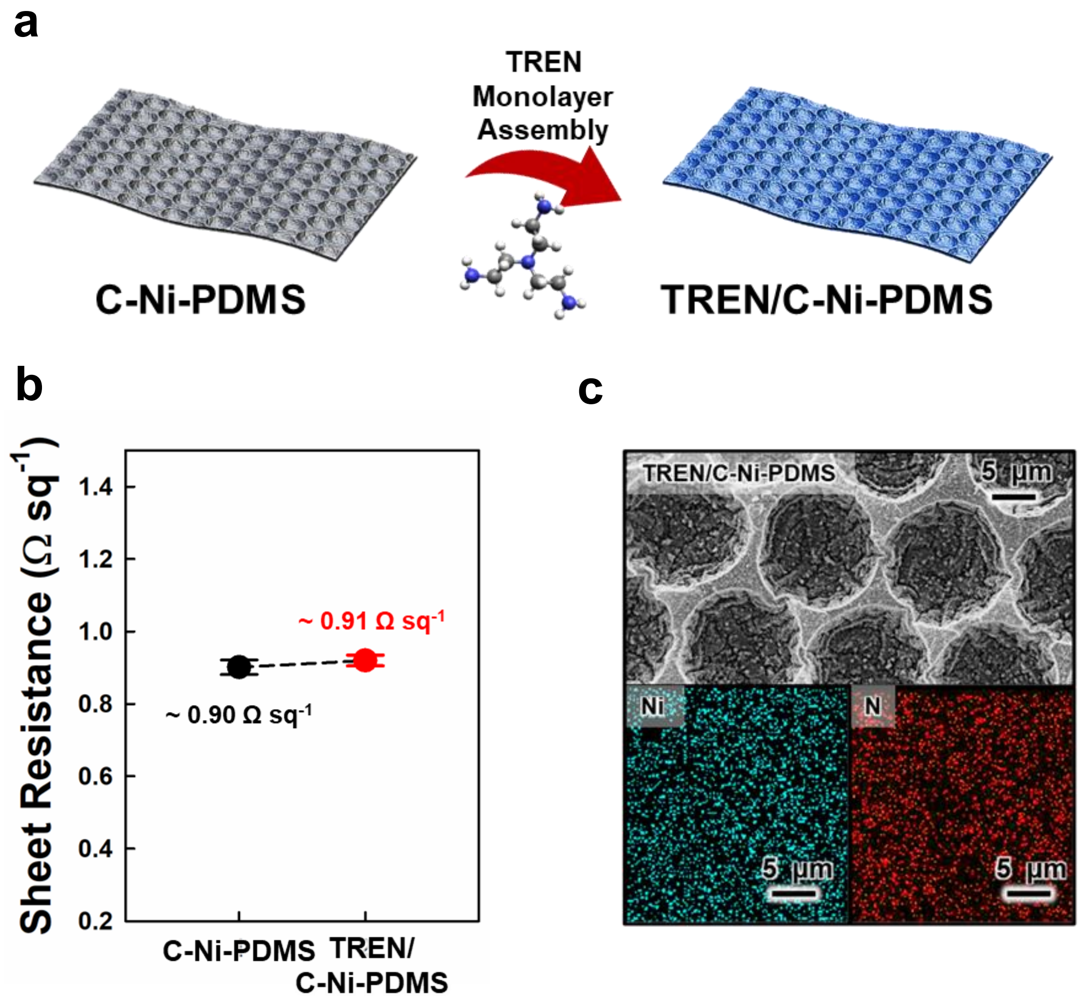

Figure S24. a) Schematic illustration of the process for TREN monolayer assembly. b) Changes in sheet resistance of C-Ni-PDMS before and after TREN molecule deposition, showing no change in electrical property (left). c) FE-SEM and corresponding EDS elemental mapping images of TREN/C-Ni-PDMS (right).

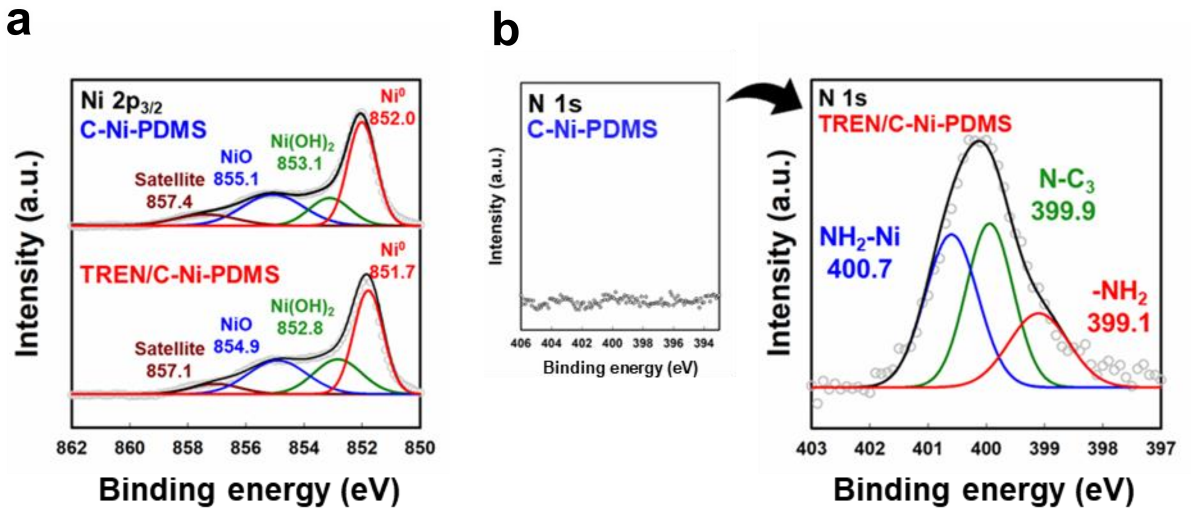

Figure S25. a) Ni $2p_{3/2}$ and b) N 1s XPS spectra of the C-Ni-PDMS after TREN coating. In this case, XPS analysis of the Ni $2p_{3/2}$ region reveals a negative shift of all components for the TREN-treated surface relative to pristine Ni-PDMS, including peaks at 852.0 eV (Ni^0), 853.1 eV ($Ni(OH)_2$), and 855.1 eV (NiO). This negative shift indicates strong electronic interactions between the electron-donating amine groups of TREN and the Ni surface. When combined with the intrinsic lithiophilicity of oxidized Ni species, these interactions further reduce the Li nucleation barrier. The N 1s spectra further confirm the successful grafting of TREN, exhibiting characteristic peaks at 400.7 eV (NH_2–Ni), 399.9 eV (N–C_3), and 399.1 eV (–NH_2).

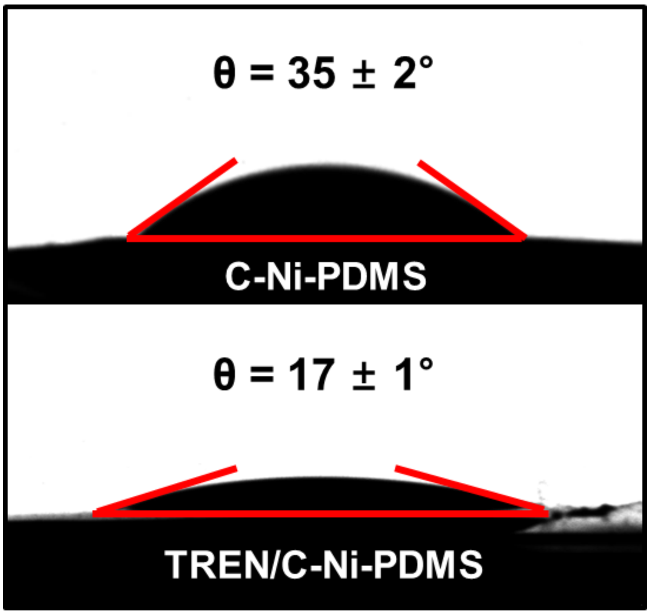

Figure S26. Electrolyte (1 M LiTFSI in DME/DOL (1:1) with 5 wt% $LiNO_3$) contact angle measurements of C-Ni-PDMS and TREN/C-Ni-PDMS.

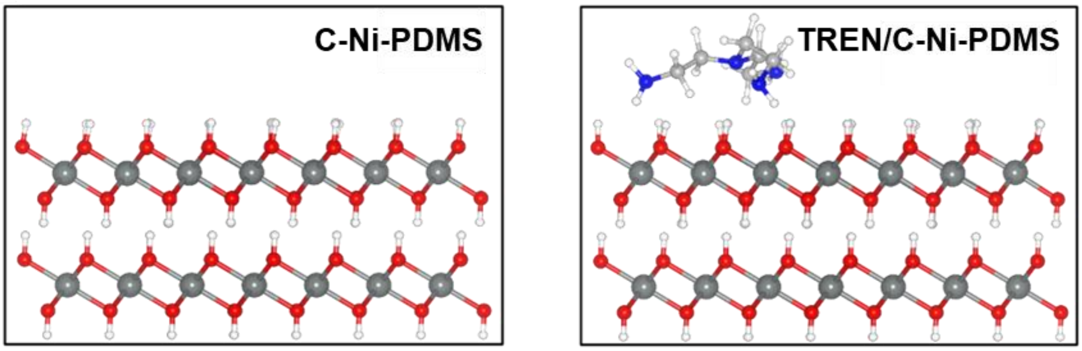

Figure S27. Atomic structure of the C-Ni-PDMS (Ni(OH)$_2$) and TREN/C-Ni-PDMS (TREN/Ni(OH)$_2$) slabs.

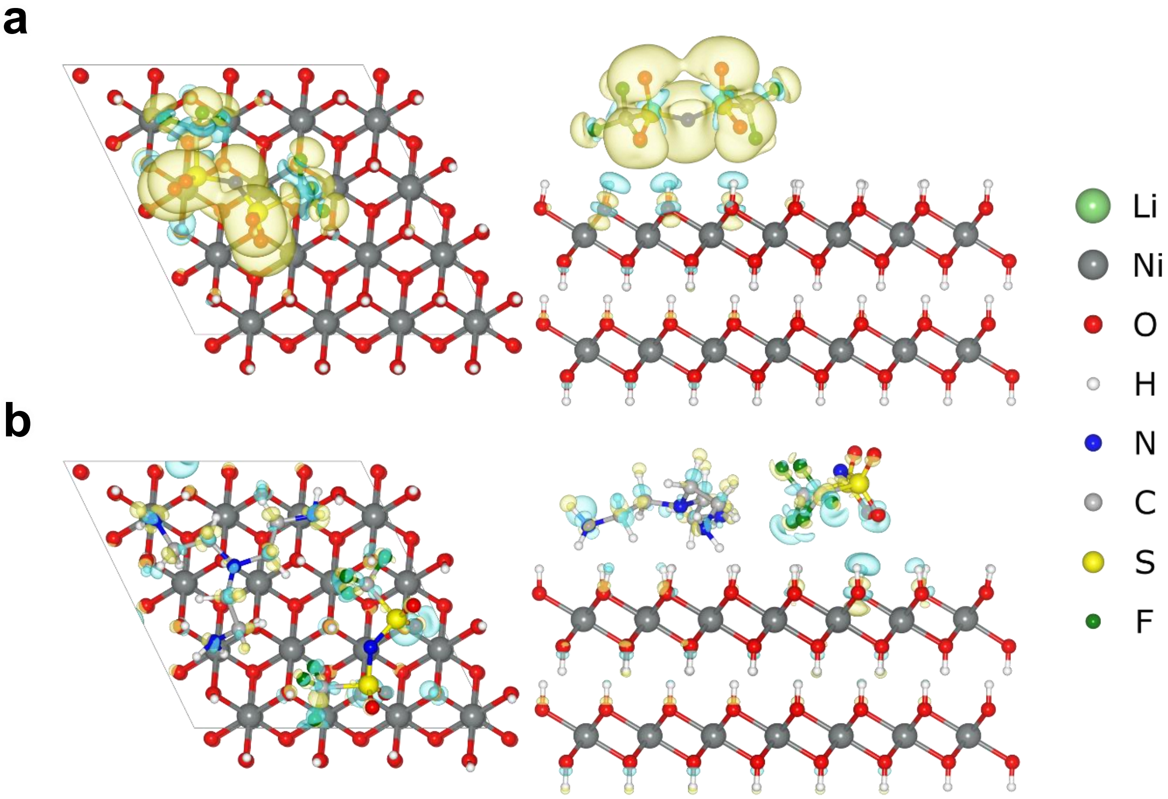

Figure S28. Charge Density Difference (CDD) analysis of TFSI$^-$ adsorption on the a) C-Ni-PDMS and b) TREN/C-Ni-PDMS. Each panel displays the top view (left) and the side view (right). The iso-surface level is set to 0.005 e/Å^3. Yellow and cyan colored regions indicate electron accumulation and depletion, respectively.

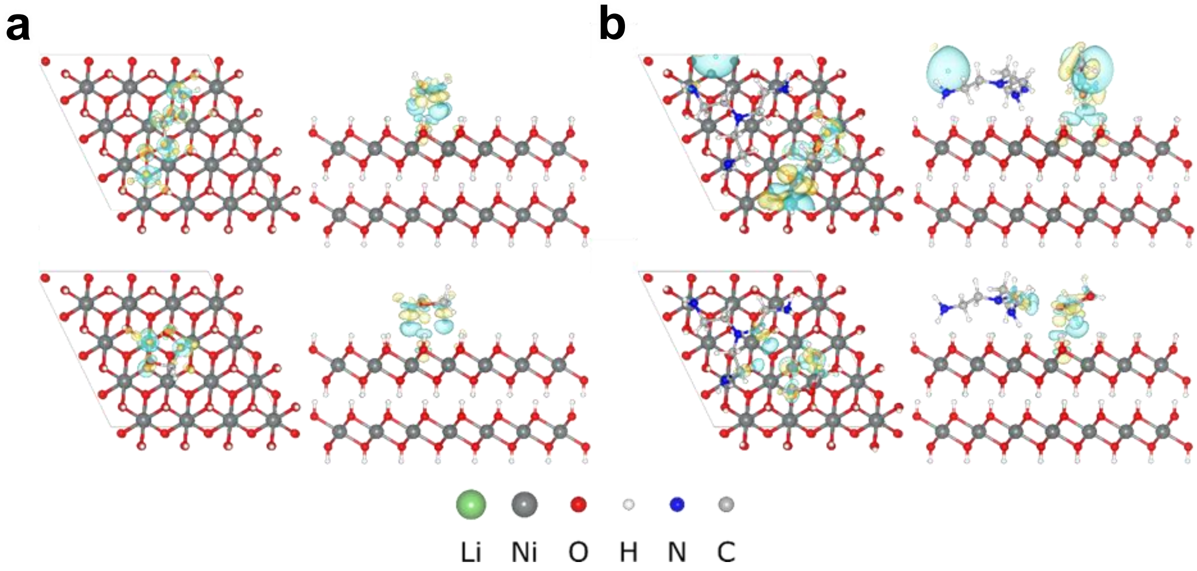

Figure S29. CDD analysis of DME and DOL solvent molecule adsorption on the a) C-Ni-PDMS and b) TREN/C-Ni-PDMS surfaces. Each panel displays the top view (left) and the side view (right). The iso-surface level is set to 0.005 e/Å^3. Yellow and cyan colored regions indicate electron accumulation and depletion, respectively.

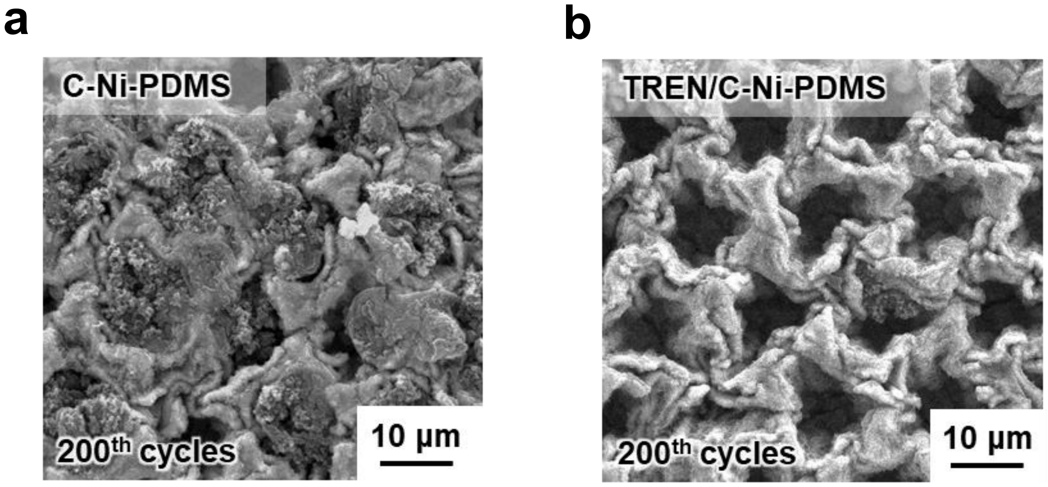

Figure S30. Top-view FE-SEM images of a) C-Ni-PDMS and b) TREN/C-Ni-PDMS electrode-based half-cells after complete Li stripping to 1.0 V (vs. Li/Li$^+$) following 200 Li plating/stripping cycles at 1 mA cm^{-2} and 1 mAh cm^{-2}.

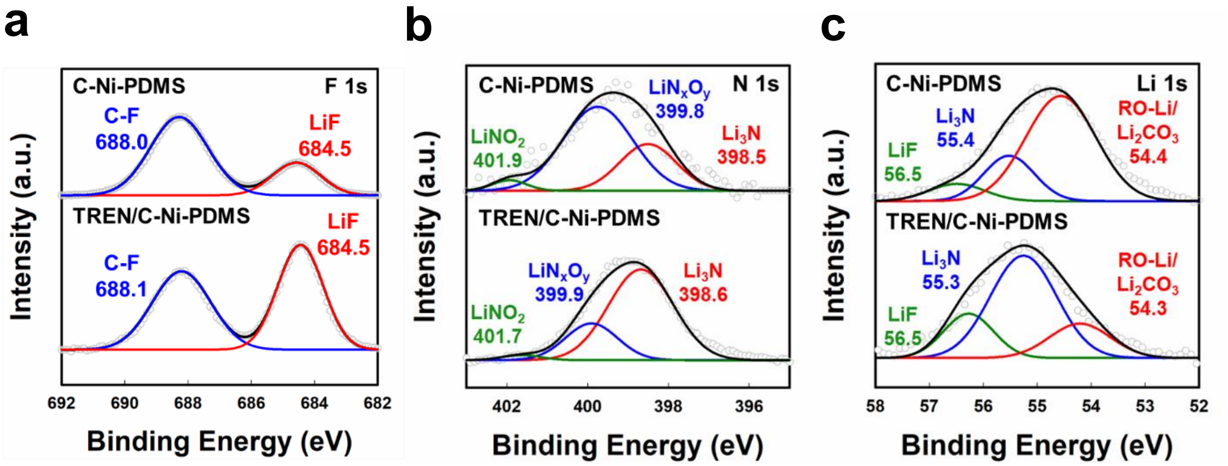

Figure S31. a) F 1s, b) N 1s and c) Li 1s XPS spectra of C-Ni-PDMS and TREN/C-Ni-PDMS-based symmetric cells after 10 cycles of Li plating/stripping. In general, amine or amide groups can form hydrogen bonds with anions such as $TFSI^-$, thereby selectively promoting their decomposition into inorganic species, including LiF. Accordingly, the lithiophilic $–NH_2$ groups in TREN are expected to interact with Li^+ and neighboring $TFSI^–$ anions at the electrode/electrolyte interface, directing a preferential LiF-forming pathway over organic decomposition. This targeted interfacial decomposition not only increases the inorganic content of the solid-electrolyte interphase (SEI) but also suppresses parasitic side reactions and facilitates uniform Li nucleation during repeated cycling.

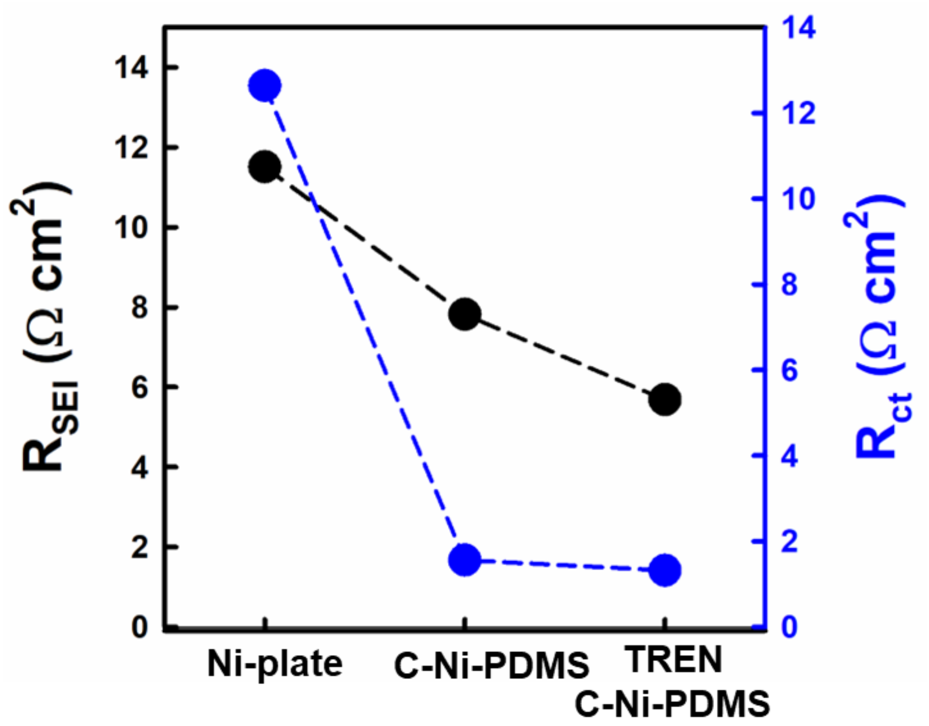

Figure S32. R_{SEI} and R_{ct} values of Ni plate, C-Ni-PDMS, and TREN/C-Ni-PDMS symmetric cells after 10 cycles of Li plating/stripping at 1 mA cm^{-2} with a capacity of 1 mAh cm^{-2}.

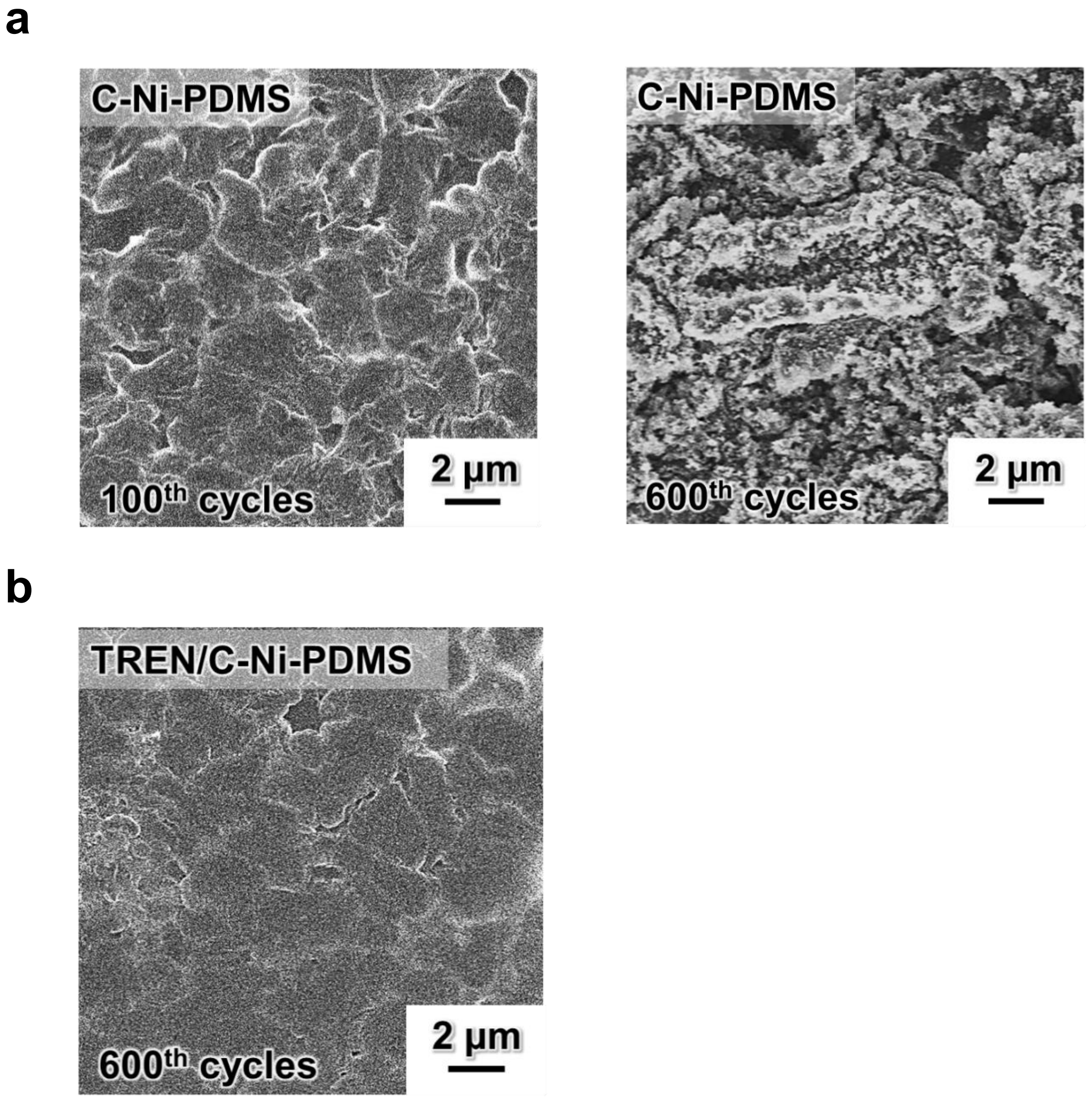

Figure S33. Top-view FE-SEM images of a) C-Ni-PDMS after 100 and 600 cycles, and b) TREN/C-Ni-PDMS after 600 cycles at 1 mA cm^{-2} and 1 mAh cm^{-2}. After 600 cycles, the C-Ni-PDMS electrode exhibits pronounced surface coarsening accompanied by irregular porous features, whereas the TREN/C-Ni-PDMS electrode maintains a compact, dendrite-free morphology. These results demonstrate that the TREN-enabled surface chemistry effectively stabilizes the solid-electrolyte interphase (SEI), suppresses repetitive SEI reformation, and mitigates interfacial degradation during prolonged cycling.

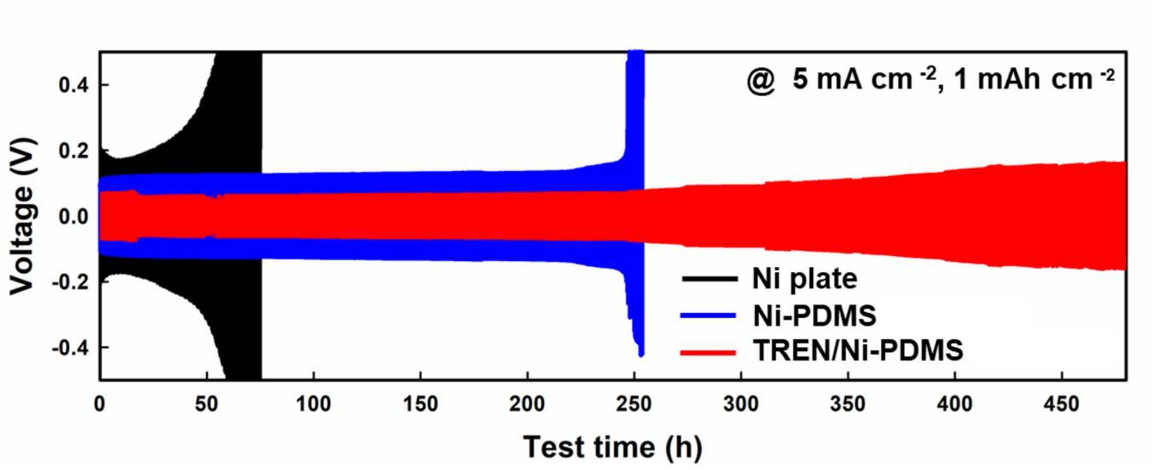

Figure S34. Galvanostatic cycling of Ni plate, C-Ni-PDMS, and TREN/C-Ni-PDMS symmetric cells at 5 mA cm^{-2} with a capacity of 1 mAh cm^{-2}.

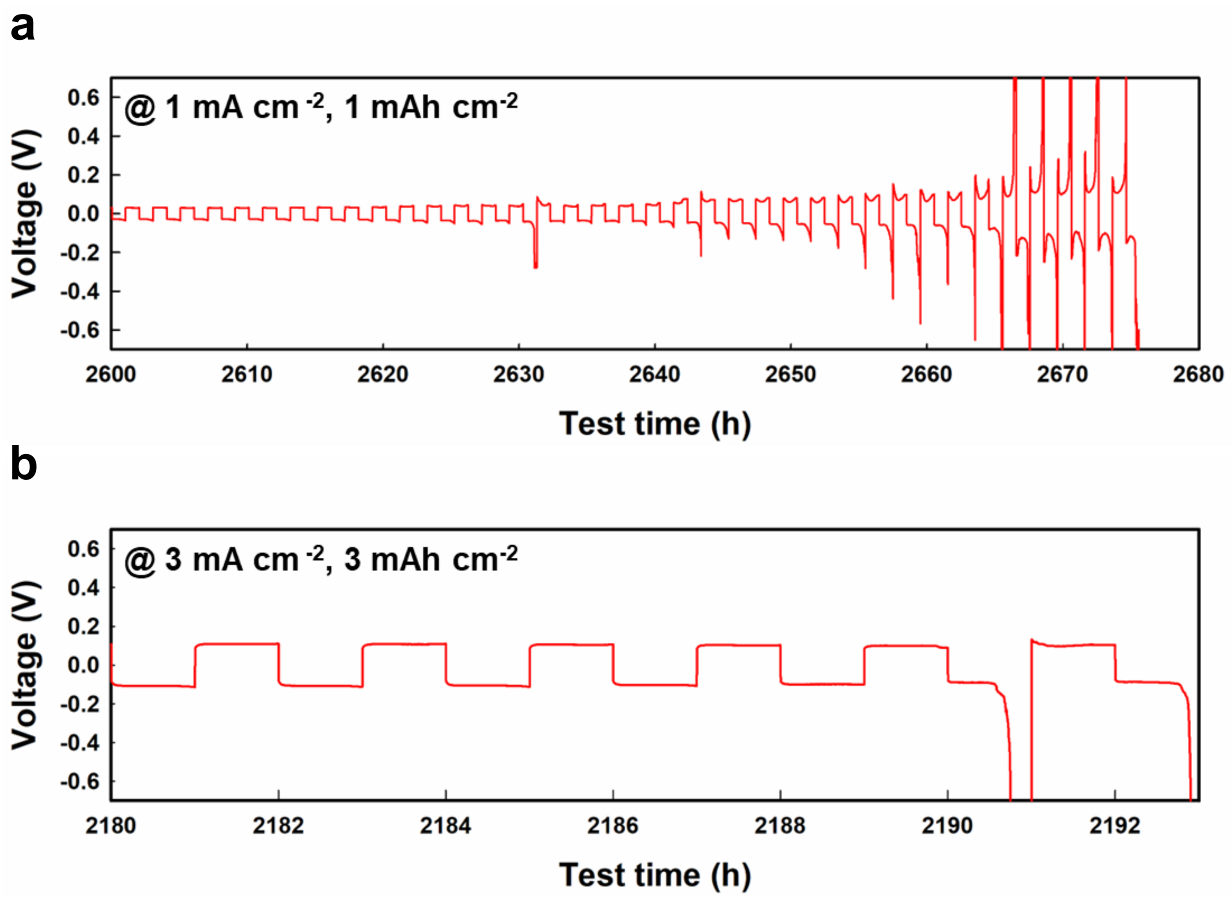

Figure S35. Galvanostatic cycling of TREN/C-Ni-PDMS symmetric cells showing short-circuit failure at a) 1 mA cm^{-2}/1 mAh cm^{-2} and b) 3 mA cm^{-2}/3 mAh cm^{-2}.

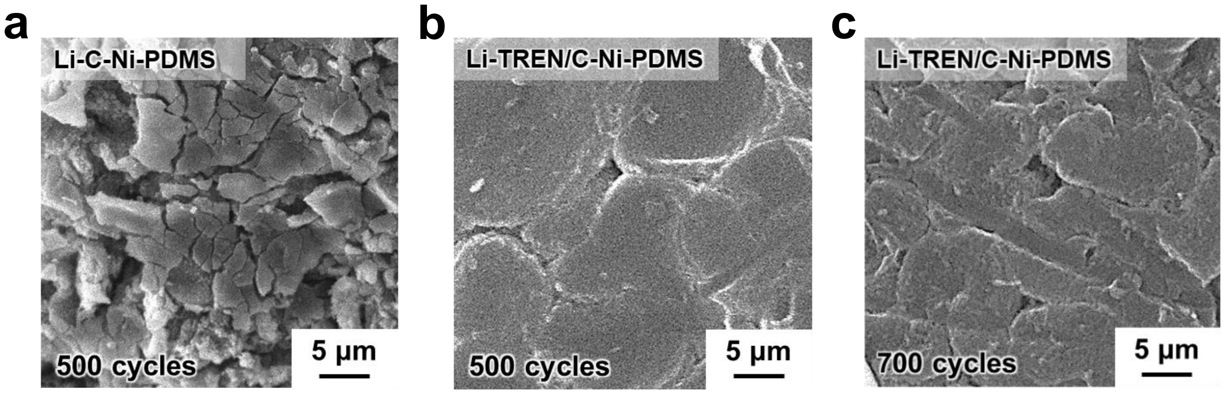

Figure S36. FE-SEM images of a) Li-C-Ni-PDMS and b) Li-TREN/C-Ni-PDMS anodes after galvanostatic charge-discharge (GCD) cycles at 1 C in a full-cell configuration. In this case, the cycled samples were collected after short-circuit failure in Li-C-Ni-PDMS-based full cells to enable a clear comparison of surface morphology. In contrast to the Li-TREN/C-Ni-PDMS anode, which maintains smooth and uniform Li deposition even after 700 GCD cycles, the Li-C-Ni-PDMS anode exhibits randomly grown Li dendrites that penetrate the separator, ultimately leading to severe cell failure after approximately 500 GCD cycles.

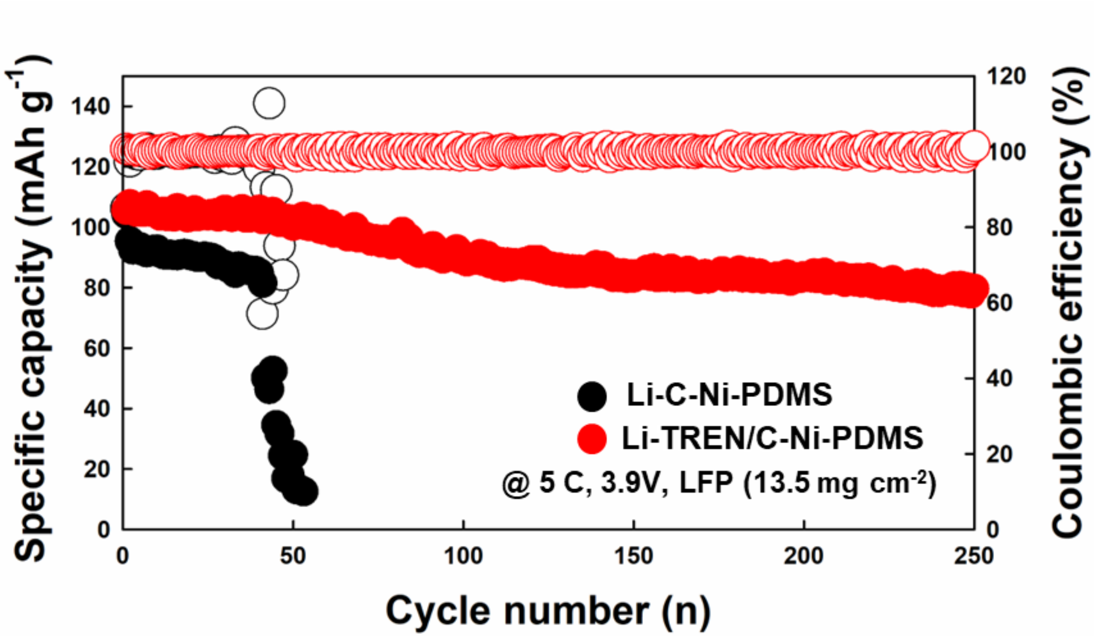

Figure S37. GCD cycling of Li-C-Ni-PDMS, Li-TREN/C-Ni-PDMS // LFP full cells measured at 5 C.

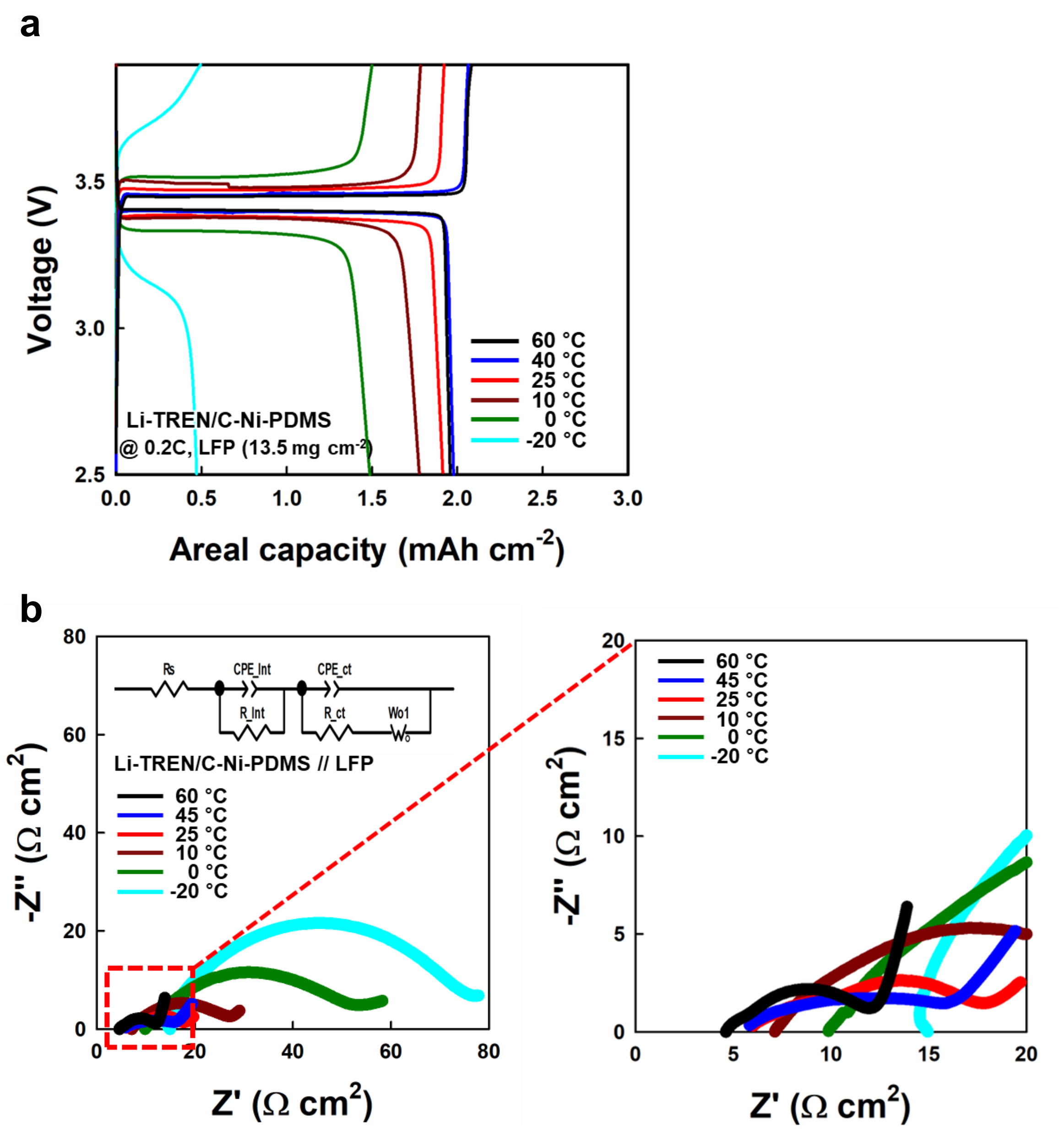

Figure S38. a) Operating temperature-dependent galvanostatic charge–discharge profiles of anode-free TREN/C-Ni-PDMS // LFP full cells measured at 0.2 C (2.3 mAh cm^{-2}) over a temperature range from -20 to 60 °C. b) Temperature-dependent Nyquist plots of the corresponding cells. The inset shows the equivalent circuit model used for data fitting and magnified view of the high-to-medium frequency region of the Nyquist plots.

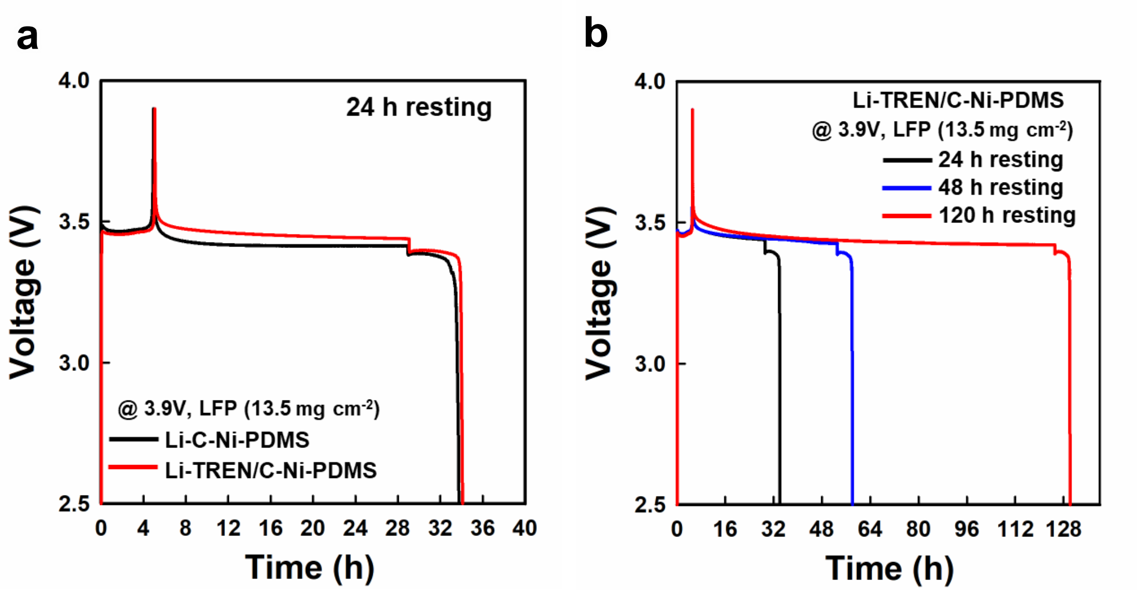

Figure S39. Self-discharge behavior of Li–TREN/C-Ni-PDMS // LFP and Li/C-Ni-PDMS // LFP full-cells at room temperature.

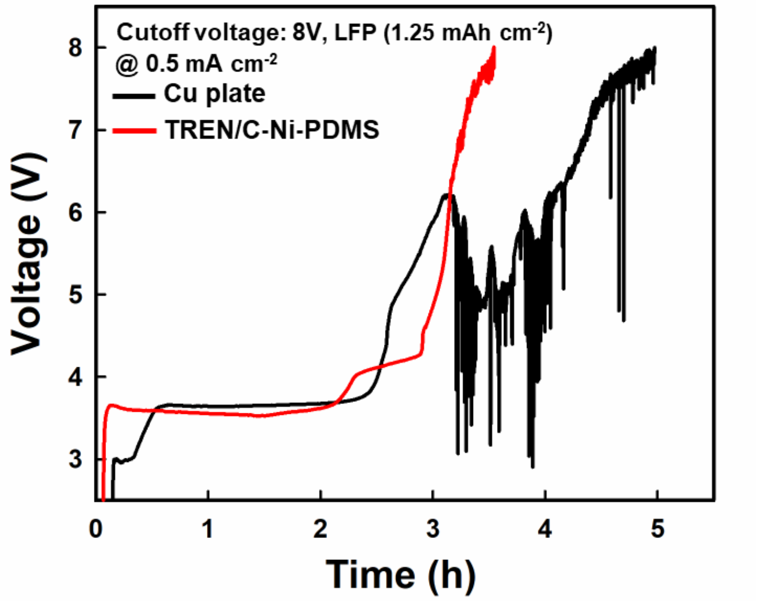

Figure S40. Voltage profiles of LFP cathode-based full cells paired with Cu plate and TREN/C-Ni-PDMS anodes during overcharge tolerance testing at 0.5 mA cm^{-2} with an extended cutoff voltage of 8 V.

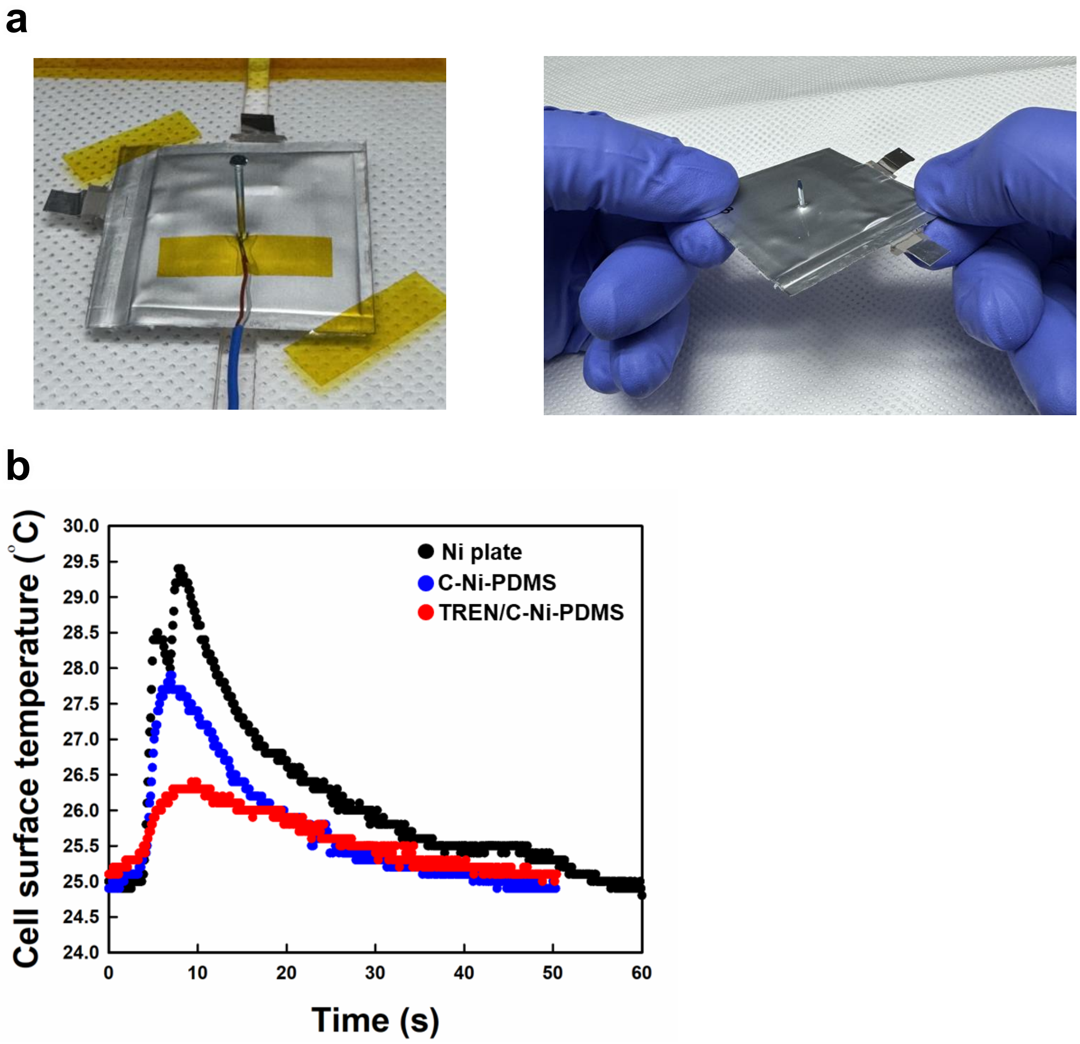

Figure S41. a) Digital images of a pouch cell with a thermocouple attached after nail penetration. b) Surface temperature profiles of pouch cells with Ni plate, C-Ni-PDMS, TREN/C-Ni-PDMS during the nail penetration test.

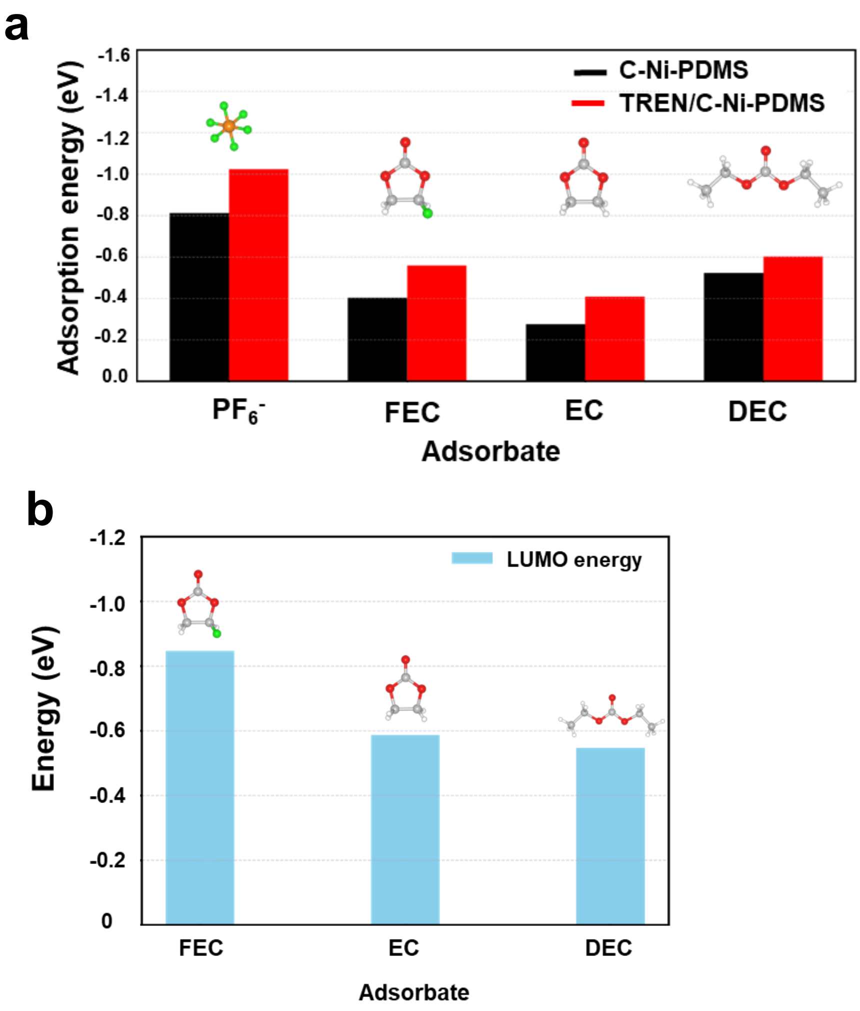

Figure S42. a) The calculated adsorption energies of PF_6^- anion, FEC additive and solvent molecules (EC and DEC) on $Ni(OH)_2$ and TREN/$Ni(OH)_2$ surfaces. b) Comparison of the lowest unoccupied molecular orbital (LUMO) energy of FEC additive and solvent molecules (EC and DEC).

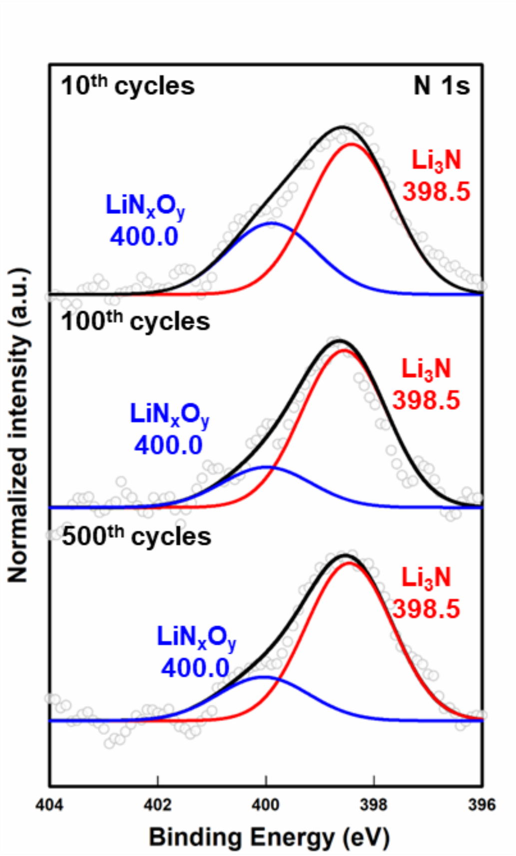

Figure S43. N 1s XPS spectra of the Li-TREN/C-Ni-PDMS anode after the 10th, 100th, and 500th galvanostatic charge-discharge cycles. The spectra were deconvoluted into contributions from Li_3N (~398.5 eV) and LiN_xO_y (~400.0 eV). The dominant Li_3N component is consistently maintained during prolonged cycling, indicating continuous formation of an anion-derived inorganic SEI and suppressed accumulation of nitrogen-containing byproducts.

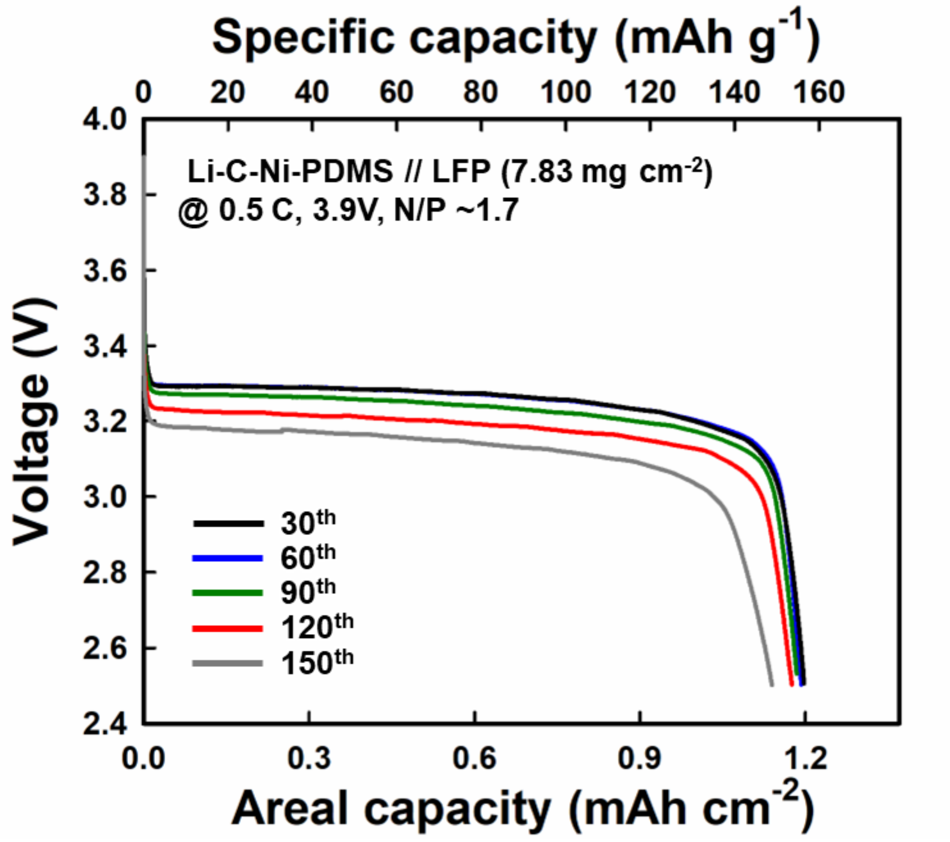

Figure S44. Cycling-dependent areal and specific capacities of Li-C-Ni-PDMS//LFP full cells (N/P ≈ 1.7)

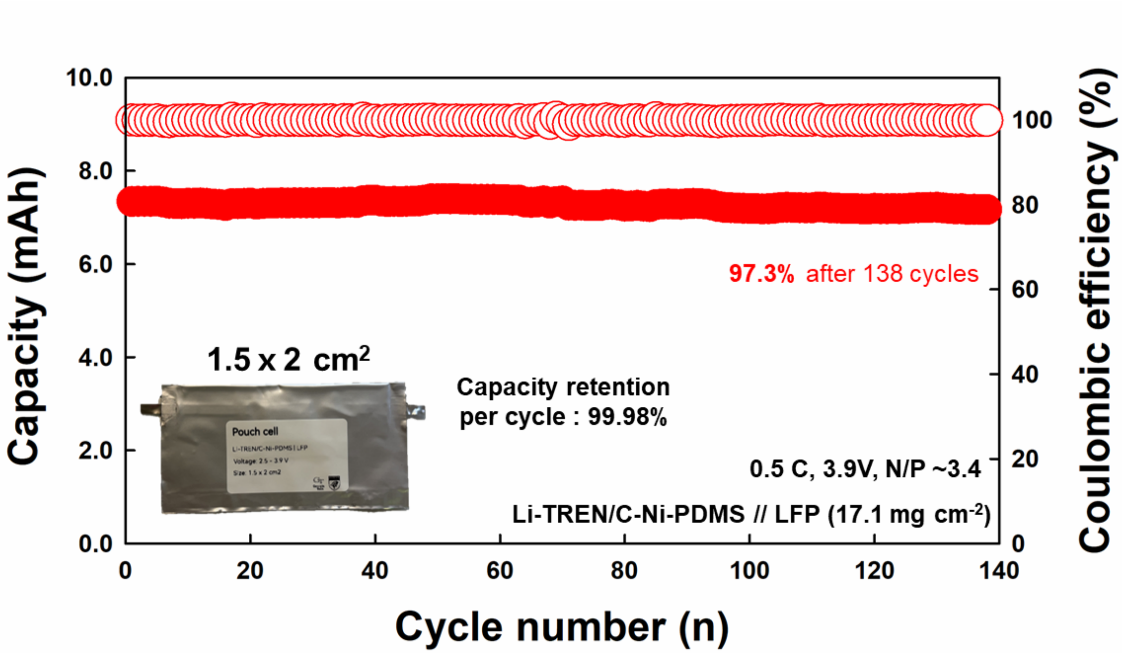

Figure S45. Cycling performance of a high-loading $LiFePO_4$ (LFP) pouch full cell (1.5 × 2 cm^2) employing the Li-TREN/C-Ni-PDMS anode, delivering a discharge capacity of ~7.4 mAh with a cathode loading of 17.1 mg cm^{-2} and stable cycling over 138 cycles.

Table S1. Comparison of cycling performance between the TREN/C-Ni-PDMS and other 3D current collectors.

System	Method	Li|Li symmetric cell performance	Full cell performance	Reference
TREN/C-Ni-PDMS	**Layer-by-layer assembly** **Electroplating**	**2,600 h @ 1mA cm^{-2}/ 1mAh cm^{-2}** **~2,200 h @ 3mA cm^{-2}/ 3mAh cm^{-2}**	**LFP: 90.1% @ 1,000 cycles (1C)**	**Our work**
Co_3O_4@NF	MOF-derived nanoarray growth	1,000 h @ 1mA cm^{-2}/ 1mAh cm^{-2}	LFP: 99 % @ 200 cycles (1C)	[S21]
Li-B@SSM	Roll-to-roll mechanical pressing	450 h @ 3mA cm^{-2}/ 3mAh cm^{-2}	LFP: 97.5% @ 400 cycles (1C)	[S22]
MCNCF	Electrodeposition, Plasma conversion,	1,200 h @ 1mA cm^{-2}/ 1mAh cm^{-2}	LFP: 99 % @ 250 cycles (1C)	[S23]
3D Cu nanowire matrix	Etching, Electroplating, Sputtering	2,160 h @ 1 mA cm^{-2}/1 mAh cm^{-2} 600 h @ 3 mA cm^{-2}/3 mAh cm^{-2}	-	[S24]
Sn@Cu foam	Laser ablation, PLD	1,500 h @ 1 mA cm^{-2}/1 mAh cm^{-2}	LFP: 97 % @ 300 cycles (1C)	[S25]
EBG CC (Cu-Ag NWs)	Layer-by-layer filtration, H_2 sintering	1,000 h @ 1 mA cm^{-2}/1 mAh cm^{-2}	LFP: 92.5 % @ 250 cycles (1C)	[S26]
CNF-CoP/Co_2P	Electrospinning, Carbonization	600 h @ 3 mA cm^{-2} / 1 mAh cm^{-2}	LFP: 89.5% @ 500 cycles (1C)	[S27]
ANCFP	Carbonization	600 h @ 1 mA cm^{-2} / 1 mAh cm^{-2}	LFP: 85% @ 300 cycles (1 C)	[S28]

NCH@CF	Electrospinning Carbonization	1,200 h @ 1 mA cm^{-2} / 1 mAh cm^{-2} 500 h @ 3 mA cm^{-2}/ 3 mAh cm^{-2}	LFP: 90% @ 150 cycles (1C)	[S29]
FCMF	Carbonization, CVD	2,000 h @ 1mA cm^{-2}/ 1mAh cm^{-2}	LFP: 85.6 % @ 400 cycles (2C)	[S30]
Zn/ZnO/Zn(CN)$_2$@C	Carbonization of MOF	900 h @ 1mA cm^{-2}/ 1mAh cm^{-2}	LFP: 94.3 % @ 200 cycles (1C)	[S31]
Cation-loaded porous Mg^{2+}-Zeolite layer	Ion-exchange Slurry casting	2100 h @ 1mA cm^{-2}/ 1mAh cm^{-2}	LFP: 91 % @ 1000 cycles (1C)	[S32]
GDD-CH	Layer-by-layer Bottom-up	1500 h @ 1mA cm^{-2}/ 1mAh cm^{-2}	LFP: 82.7 % @ 300 cycles (1C)	[S33]
NSNF	Selenization Mechanical rolling	600 h @ 3 mA cm^{-2}/ 3 mAh cm^{-2}	LFP: 95.4 % @ 500 cycles (1C)	[S34]
3D CuZrAg MG	Melt-spinning, Dealloying	2,000 h @ 1mA cm^{-2}/ 1mAh cm^{-2}	LFP: 92 % @ 600 cycles (1C)	[S35]
Ag@CuO	Hydrothermal growth Oxidation	1,100 h @ 1mA cm^{-2}/ 1mAh cm^{-2}	LFP: ~70% @ 210 cycles (1C)	[S36]
NCNF@MoP	Electrospinning, Phosphorization	2,500 h @ 1mA cm^{-2}/ 1mAh cm^{-2} 560 h @ 3 mA cm^{-2}/ 3 mAh cm^{-2}	LFP: 88% @ 1000 cycles (1C)	[S37]
CNF-CoO$_x$	Electrospinning, Carbonization, Reduction	~400 h @ 3 mA cm^{-2}/ 1 mAh cm^{-2}	LFP: ~89% @ 480 cycles (1C)	[S38]

Supplementary References

[S1] S. G. Booth, A. Uehara, S. Y. Chang, C. La Fontaine, T. Fujii, Y. Okamoto, T. Imai, S. L. M. Schroeder, R. A. W. Dryfe, *Chem. Sci.* **2017**, *8*, 7954.

[S2] J. Zhang, Y. Chen, M. A. Brook, *Langmuir* **2013**, *29*, 12432.

[S3] G. Kresse, J. Hafner, *Phys. Rev. B* **1993**, *48*, 13115.

[S4] G. Kresse, J. Furthmüller, *Comput. Mater. Sci.* **1996**, *6*, 15.

[S5] P. E. Blöchl, *Phys. Rev. B* **1994**, *50*, 17953.

[S6] G. Kresse, D. Joubert, *Phys. Rev. B* **1999**, *59*, 1758.

[S7] J. Moellmann, S. Grimme, *J. Phys. Chem. C* **2014**, *118*, 7615.

[S8] S. Grimme, S. Ehrlich, L. Goerigk, *J. Comput. Chem.* **2011**, *32*, 1456.

[S9] H. J. Monkhorst, J. D. Pack, *Phys. Rev. B* **1976**, *13*, 5188.

[S10] S. L. Dudarev, G. A. Botton, S. Y. Savrasov, C. J. Humphreys, A. P. Sutton, *Phys. Rev. B* **1998**, *57*, 1505.

[S11] A. Jain, S. P. Ong, G. Hautier, W. Chen, W. D. Richards, S. Dacek, S. Cholia, D. Gunter, D. Skinner, G. Ceder, K. A. Persson, *APL Mater.* **2013**, *1*, 011002

[S12] Y. H. Yun, K. Kim, C. Lee, B.-S. An, J. H. Kwon, S. Lee, M. Kim, J. Seo, J. H. Park, B.-H. Kim, H.-S. Cho, *J. Energy Chem.* **2023**, *82*, 560.

[S13] K. Mathew, V. S. C. Kolluru, S. Mula, S. N. Steinmann, R. G. Hennig, *J. Chem. Phys.* **2019**, *151*, 234101

[S14] K. Mathew, R. Sundararaman, K. Letchworth-Weaver, T. A. Arias, R. G. Hennig, *J. Chem. Phys.* **2014**, *140*, 084106

[S15] J. Liu, R. Lu, G. Xiao, C. Zhang, K. Zhao, Q. He, Y. Zhao, *J. Colloid Interface Sci.* **2022**, *616*, 886.

[S16] Y. Liu, Y. Tian, F. Kang, M. Wagemaker, B. Li, G. Chen, *Adv. Funct. Mater.* **2026**, *36*, e19229.

[S17] K. S. Han, J. Chen, R. Cao, N. N. Rajput, V. Murugesan, L. Shi, H. Pan, J.-G. Zhang, J. Liu, K. A. Persson, K. T. Mueller, *Chem. Mater.* **2017**, *29*, 9023.

[S18] Y. Liu, X. Xu, M. Sadd, O. O. Kapitanova, V. A. Krivchenko, J. Ban, J. Wang, X. Jiao, Z. Song, J. Song, S. Xiong, A. Matic, *Adv. Sci.* **2021**, *8*, 2003301.

[S19] J. J. Hu, G. K. Long, S. Liu, G. R. Li, X. P. Gao, *Chem. Commun.* **2014**, *50*, 14647.

[S20] E. Cossar, M. S. E. Houache, Z. Zhang, E. A. Baranova, *J. Electroanal. Chem.* **2020**, *870*, 114246.

[S21] Y. Wang, X. Li, L. Wu, J. Tan, G. Liu, C. Ye, L. Ma, Z. Liu, M. Ye, J. Shen, *Energy Storage Mater.* **2024**, *66*, 103247

[S22] P. Qing, Z. Wu, A. Wang, S. Huang, K. Long, T. Naren, D. Chen, P. He, H. Huang, Y. Chen, L. Mei, L. Chen, *Adv. Mater.* **2023**, *35*, 2211203.

[S23] X. Wang, Z. Chen, X. Xue, J. Wang, Y. Wang, D. Bresser, X. Liu, M. Chen, S. Passerini, *Nano Energy* **2025**, *133*, 110439.

[S24] X. Zhu, H. Cheng, S. Lyu, J. Huang, J. Gu, Y. Guo, Y. Peng, J. Liu, C. Wang, J. Duan, S. Yang, *Adv. Energy Mater.* **2023**, *13*, 2300129.

[S25] Y. Hui, Y. Wu, W. Sun, X. Sun, G. Huang, Z. Na, *Adv. Funct. Mater.* **2023**, *33*, 2303319.

[S26] J. Chen, S. Zhang, Y. Huang, X. Han, H. Li, G. Liu, L. Shi, Y. Zhang, Z. Shen, Y. Wang, Y. Ma, J. Zhao, *Adv. Funct. Mater.* **2025**, *35*, 2500531.

[S27] Z. Hao, D. Liu, X. Zuo, H. Yu, T. You, Y. Zhang, *Adv. Funct. Mater.* **2025**, *35*, 2415251.

[S28] Y.-K. Lee, K.-Y. Cho, S. Lee, J. Choi, G. Lee, H.-I. Joh, K. Eom, S. Lee, *Adv. Energy Mater.* **2023**, *13*, 2203770.

[S29] C. Chen, J. Guan, N. W. Li, Y. Lu, D. Luan, C. H. Zhang, G. Cheng, L. Yu, X. W. Lou, *Adv. Mater.* **2021**, *33*, 2100608.

[S30] J. Liao, S. Huang, Z. Xie, A. Wang, A. Zhu, H. Huang, W. Li, Z. He, R. Xia, Z. Wu, P. Qing, L. Chen, *Adv. Funct. Mater.* **2025**, *35*, 2506529.

[S31] M. Song, Y. Li, L. Gao, R. Zhao, Y. Xu, S. Han, J. Zhu, L. Wang, Y. Zhao, *Small* **2024**, *20*, 2306187.

[S32] B. Su, X. Wang, L. Chai, S. Huo, J. Qiu, Q. Huang, S. Li, Y. Wang, W. Xue, *Adv. Sci.* **2024**, *11*, 2308939.

[S33] Y. Zhang, M. Yao, T. Wang, H. Wu, Y. Zhang, *Angew. Chem. Int. Ed.* **2024**, *63*, e202403399.

[S34] C. Li, C. Yang, T. Huang, Y. Wang, J. Yang, Y. Jiang, J. Mao, S. Zheng, S. Xia, *Adv. Funct. Mater.* **2024**, *34*, 2407149.

[S35] P. Ye, Y. Zhang, T. Tong, L. Ao, Z. Chen, H. Huang, A. Hussain, A. Ramiere, X. Cai, D. Liu, J. Shen, *Small* **2023**, *19*, 2304373.

[S36] M. Gao, Q. Dong, M. Yao, X. Wang, J. Li, W. Zhang, H. Huang, H. Guo, Z. Sun, Q. Chen, X. Han, W. Hu, *Adv. Funct. Mater.* **2024**, *34*, 2401442.

[S37] D. Chen, C. Chen, H. Yu, S. Zheng, T. Jin, N. W. Li, L. Yu, *Adv. Funct. Mater.* **2024**, *34*, 2402951.

[S38] Z. Hao, D. Liu, X. Zuo, H. Yu, Y. Zhang, *Adv. Mater.* **2024**, *36*, 2404983.